Ore Geology Reviews 148 (2022) 105004

Contents lists available at ScienceDirect

Ore Geology Reviews

journal homepage: www.elsevier.com/locate/oregeorev

Tectonic control on the spatial distribution of Sn mineralization in the Gejiu Sn district, China

Rong Xu [a,b], Rolf L. Romer [b], Uwe Kroner [c], Jun Deng [a,*]

[a] State Key Laboratory of Geological Processes and Mineral Resources, School of Earth Sciences and Resources, China University of Geosciences, Beijing 100083, China
[b] Inorganic and Isotope Geochemistry, GFZ German Research Centre for Geosciences, Telegrafenberg, D-14473 Potsdam, Germany
[c] TU Bergakademie Freiberg, Department of Geology, B. v. Cotta Str. 2, D-09596 Freiberg, Germany

ARTICLE INFO

Keywords:
Granites
Sn deposits
Orientation of stress field
Ailaoshan Fault Zone
Gejiu Sn district

ABSTRACT

Late Cretaceous granitic rocks occur in the Gejiu ore district to the east and west of the N-S striking Gejiu Fault, whereas major Sn deposits are only known to occur to the east of the Gejiu Fault. Comparison of the whole-rock chemistry, the apatite trace-element chemistry, and zircon Hf and O isotope data of the various granites demonstrates that fertile granites occur to both sides of the Gejiu fault. The results demonstrate that the c. 83 Ma old granitic intrusions (i) have similar magma sources, which are dominated by metasedimentary rocks that had experienced intense chemical weathering, resulting in reduced melts, (ii) had similar melting conditions, i.e., high temperature biotite dehydration melting, and (iii) in part had experienced large extents of fractional crystallization. The most evolved granites to both sides of the Gejiu Fault have the characteristics typical of tin granites. Therefore, the absence of major deposits to the west of the Gejiu Fault is not due to the absence of fertile granites. The areas to the east and the west of the Gejiu Fault, however, have fundamentally different fault pattern, which indicates different orientation of the stress field to both sides of the Gejiu Fault at the time of the emplacement of the Cretaceous granites. Late Cretaceous dextral movement along the Ailaoshan Fault Zone resulted in a (trans)tensional setting in areas to the east of the Gejiu Fault and in a (trans)pressional setting to the west of that fault. We speculate that the tectonic setting influences the potential for mineralization because the Sn bearing fluids need efficient pathways to transporting metals from the roof zone of the batholith into the wall rocks. In contrast to regional compression, hydraulic fracturing in an overall extensional setting has the potential to develop efficient fluid pathways and, thus, may lead to major ore deposits. To the west of the Gejiu Fault, however, granite intrusions in an overall compressional setting are likely to develop no or only small mineralization.

1. Introduction

The Gejiu tin polymetallic ore district is the largest known primary Sn accumulation in the world, with an estimated endowment of 3.2 Mt of Sn, 3.3 Mt of Cu, 5.2 Mt of Pb + Zn, and more than 0.2 Mt of W. There are five types of Sn mineralization, i.e., (i) Sn − Cu ore within altered granites, (ii) Sn − Cu ± W skarn ore, (iii) Sn greisen ore, (iv) carbonate-hosted stratiform Sn − Pb ± Zn ± Cu ore, and (v) carbonate-hosted tourmaline veins with Sn − Be − W ore (Cheng et al., 2013a; Zhang et al., 2020; Xu et al., 2021). The Gejiu district includes two areas of contrasting surface geology and mineralization that are separated by the N-S striking Gejiu Fault. To the east of the fault, surface exposures are dominated by Triassic carbonates, whereas to the west of the fault different types of Late Cretaceous magmatic rocks predominate (Fig. 1c). To the east of the Gejiu Fault, there are several major deposits, i.e., the Malage (Sn-Cu), the Songshujiao (Sn-Cu-Pb), the Gaosong (Sn-Pb-Zn), the Laochang (Sn-W-Cu), and the Kafang (Sn-Cu) deposits (Fig. 1c). Major mineralization is closely related to fault zones and their intersections (Jiang et al., 1997; Zhao et al, 2015). To the west of the Gejiu Fault, mineralization is only sporadic with small Pb-Sn ore bodies. The largest mined Sn-Pb ore is the Douyan deposit with an estimated endowment of 651 t of primary Sn ore and 330 t of alluvial Sn ore (308 Geological Party, 1984; He et al., 2014; Lu and Liu, 2020). The areas to the east and to the west of the Gejiu Fault not only have a different distribution of mineralization, but also contrasting fault pattern (Jiang et al., 1997; Tan et al., 2013; Zhao et al., 2015).

* Corresponding author.
E-mail address: djun@cugb.edu.cn (J. Deng).

https://doi.org/10.1016/j.oregeorev.2022.105004
Received 24 September 2021; Received in revised form 23 May 2022; Accepted 27 June 2022
Available online 2 July 2022

Primary Sn mineralization in the Gejiu district is spatially and genetically linked to Late Cretaceous granites. To the east of the Gejiu Fault, granitic intrusions are not exposed, except for a granite area (~6 km^2) to the north of the Malage deposit, but reach to a depth of 200 to 1000 m below the surface. Unexposed granitic bodies with major deposits include the Malage-Songshujiao porphyritic granite, the Laochang porphyritic granite, and the Laochang-Kafang equigranular granite. To the west of the Gejiu Fault, exposures of granitoids cover an area of ~ 320 km^2 (Fig. 1c), the most important intrusions being the Longchahe porphyritic granitic body and the Shenxianshui equigranular granitic body. In addition to these granitoids, there occur also gabbros (~10 km^2), syenites (~45 km^2), and a relatively small granitic body (~14 km^2) with abundant mafic microgranular enclaves (MMEs; Fig. 1c). Such rocks are not known to the east of the Gejiu Fault. One key question in understanding the metallogeny of the Gejiu district addresses the causes for the different distribution of mineralization. Have major deposits to the west of the Gejiu Fault not been found yet, have they been removed because a deeper crustal level is exposed, or did major deposits just not form because of differences in magma source and development or differences in tectonic setting to the east and the west of the Gejiu Fault?

Not all granites have associated Sn mineralization. Tin granites are chemically highly evolved, relatively reduced rocks that are derived from partial melting of crustal source rocks (e.g., Heinrich, 1990; Lehmann et al., 1990; Sato, 2012). Tin granites commonly show a strong enrichment in Sn, W, Be, Cs, F, B, Li, Rb, Ta, and U, a marked depletion in Fe, Ti, Mg, Ca, Sr, Eu, Ba, and Zr, and low Fe_2O_3/FeO values (e.g., Stussi, 1989; Lehmann, 1990; Breiter et al., 2005). The absence of mineralization associated with such granitic rocks could be due to a wide range of causes, including: (i) insufficient magmatic fractionation (e.g., Fogliata et al., 2012; Ballouard et al., 2016; Azadbakht et al., 2020); (ii) too low melting temperatures in the source of the granitic rocks, with Sn being concentrated in stable residual phases and leading to Sn poor melts (Romer and Kroner, 2016; Wolf et al., 2018; Yuan et al., 2019); (iii) oxidizing rather than reducing conditions during magma fractionation favoring the crystallization of magnetite and titanite that may incorporate significant amount of Sn and, thus, preventing the enrichment of Sn in residual, volatile-rich melts (Ishihara et al., 1979;

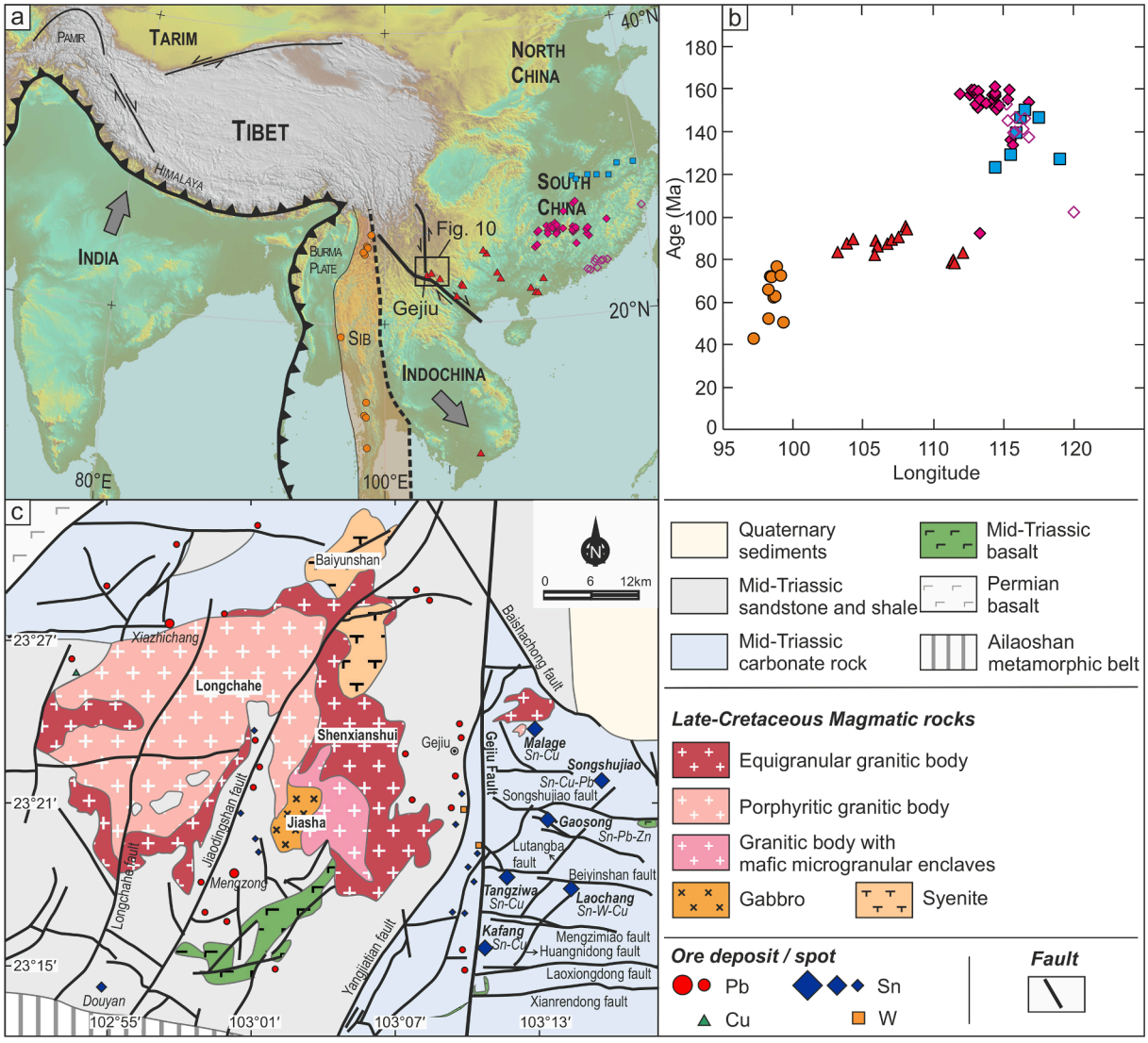

Fig. 1. (a) Map of Southeast Asia, showing the distribution of Jurassic to Tertiary Sn-(W) deposits in South China, Sibumasu, and Indochina. (b) Age (Ma) vs. longitude diagram for Sn-(W) deposits shown in Fig. 1a. To highlight the contrasting distribution of deposits of different age, Late-Triassic, Silurian, and Neoproterozoic Sn deposits are not shown. Deposits and age data are from Mao et al. (2019), Yuan et al. (2019), Hu et al. (2021), Gardiner et al. (2016), Wang et al. (2014), and Myint et al. (2021). (c) Simplified geologic map of the Gejiu district (modified after Cheng et al., 2013b; Zhang et al., 2015), showing the contrasting fault patterns and distribution of mineralization to the east and west of the Gejiu Fault. Note, most of the Late-Cretaceous granite intrusions to the east of the Gejiu Fault are not exposed. Frame in Fig. 1a indicates the area shown in the tectonic diagram in Fig. 10.

Chen et al., 1992a; Wang et al., 2013). The exsolution of magmatic fluids in highly evolved granitic systems typically results in the redistribution of metals that were incompatible during magmatic fractionation and leads to strong alteration of magmatic minerals. Fluid exsolution and alteration of the magmatic mineral assemblage result in chemical changes of the granites. Therefore, the chemical characteristics of accessory minerals that are likely to preserve their original composition such as zircon, apatite, titanite, and monazite, have been increasingly used as proxy for magma development (e.g., Ballard et al., 2002; Lu et al., 2016; Palma et al., 2019; Xing et al., 2021; Deng et al., 2020a, b).

In this paper, we study possible causes for the contrasting distribution and size of mineralization in the two areas separated by the Gejiu Fault. In a first step, we compare granitoids from the eastern and western parts of the Gejiu district, using whole rock chemistry and Nd isotope data, zircon U-Pb dating and Hf-O isotope data, and apatite major and trace element data of granitic rocks from. Based on these data we argue that (i) most granites to the west of the Gejiu Fault are not likely to produce major Sn mineralization and that (ii) a few granites to the west of the Gejiu Fault have the same chemical fingerprint as granitic rocks with important Sn mineralization to the east of the fault. The latter point indicates that the absence of major deposits to the west of the Gejiu fault is not due to the absence of fertile granites. In a second step, we discuss whether the present erosion level and the stress field at the time of granite emplacement contribute to the contrasting exposure of mineralization to the east and the west of the Gejiu Fault. Finally, we argue that the absence of major deposits to the west of the fault possibly is related to contrasting conditions of emplacement, most importantly the orientation of the local stress field.

2. Geologic setting

2.1. Regional setting of the Gejiu district

The Gejiu Sn-polymetallic ore district is located near the southwestern margin of the South China Block (Fig. 1a), which hosts several major Sn provinces. The southeastern margin of the South China Block experienced several phases of arc magmatism related to the subduction of the Paleo-Pacific plate (Hu et al., 2015). Several phases of back-arc crustal extension related to reorganization of the subduction zone resulted in the formation of major Sn and W mineralization. The most important phases of mineralization were at 160–140 and 120–100 Ma (Mao et al., 2013, 2019). To the southwest, the South China Block bordered to the Paleo-Tethys that became closed during the Triassic accretion of Sibumasu (Metcalfe, 2002; Zi et al., 2012). Intrusion of 240–220 Ma granites, locally with important Sn-W mineralization, was associated with this collision, in particular along the developing active plate margin to the SW of Sibumasu (Wai-Pan Ng et al., 2015).

The most prominent expression along the former Paleo-Tethys margin of the South China Block is the Ailaoshan Fault Zone that has been recurrently reactivated during sinistral and dextral strike-slip movements (Deng et al., 2014; Chen et al., 2019; Yang et al., 2021). Activity along the Ailaoshan Fault Zone was coeval with the accretion of magmatic arcs to mainland Asia, such as the Kohistan and Gangdese arcs, and with the collision Indian of the Indian subcontinent with mainland Asia (Searle et al., 2016; Sloan et al., 2017; Chen et al., 2019). The contrasting processes affecting the southern margin of the South China Block is also reflected in the regional variation of the ages of post-Triassic Sn mineralization (Fig. 1b). To the east, Sn mineralization falls in two age groups, i.e., 160–140 Ma and 120–100 Ma (Mao et al. 2013) and their formation seems to be controlled by the subduction of the Paleo-Pacific plate, in particular the rollback of the slab with related back-arc extension (Mao et al., 2019). To the west, Sn mineralization falls in the age range of 80–40 Ma and are mainly related to the Neo-Tethys suturing (Gardiner et al., 2015). Tin deposits along the former suture of the Paleo-Tethys, in particular along the Ailaoshan Fault Zone, and seems to related neither to the tectonics of the Paleo-Pacific plate nor the Indian plate (see also Chen et al., 2019).

2.2. Geology of the Gejiu district

The Gejiu district is near the former margin of the South China Block, i.e., the Ailaoshan Fault Zone, that was reactivated as a major strike slip fault zone during the Cretaceous and Tertiary collisions of the Kohistan and Gangdese arcs and of India, i.e., during the closure of the Meso-Tethys and the Neo-Tethys (Hu et al., 2015; Chen et al., 2019). The Gejiu district is located to the north of the Ailaoshan Fault Zone at a position where this crustal-scale tectonic element makes a kink and N-S striking Xianshuihe-Xiaojiang fault connect with the Ailaoshan Fault (Fig. 1a). The N-S striking Gejiu Fault, which is the southern extension of the regional N-S striking Xianshuihe-Xiaojiang fault, represents the dominant structure in the Gejiu ore district, separating two areas of contrasting structural style, sedimentary and magmatic rocks, and mineralization.

(i) Structural style. To the east of the N-S striking Gejiu Fault, there are three sets of faults, striking E-W, NNE-SSW, and NW-SE, respectively (Fig. 1c). The NW-SE and E-W striking faults, including Baishachong, Songshujiao, Beiyinshan, Mengzimiao, Laoxiongdong, and Xianrendong faults, are interpreted to be main pathways for the ore-forming fluids (Jiang et al., 1997). To the west of the Gejiu Fault, the dominating faults are NNE-striking, such as the Longchahe, Jiaodingshan, and Yangjiatian faults, whereas E-W and NW-SE striking faults are less developed and mainly occur in the peripheral area of the granitic intrusions (Fig. 1c). In the central part of the western area, where major granitic bodies were emplaced, E-W and NW-SE striking faults are rare.

(ii) Sedimentary and magmatic rocks. The Gejiu district has a Proterozoic metamorphic basement that is covered by Paleozoic to Mesozoic sedimentary rocks. The sedimentary sequence is incomplete: Silurian, Jurassic, and Cretaceous strata are absent. The sedimentary rocks are dominated by passive margin rocks, with interbedded Cambrian to Ordovician sandstones and dolomitic limestones (not exposed in the map area), upper Devonian to lower Permian carbonate rocks, and Triassic siltstones, shales, and carbonate rocks (Fig. 1c). In the Gejiu ore district, exposed sedimentary rocks mainly belong to the Middle Triassic Gejiu and Falang formations (Chen et al., 1992b). The Gejiu Formation consists of limestones, argillaceous limestones, and dolomitic limestones and occurs mainly to the east of the Gejiu Fault and to the north of the exposed major granitic intrusions (Fig. 1c). The Falang Formation includes siltstones and shale. It occurs to the west of the Gejiu Fault (Fig. 1c). The rocks of the Falang Formation were deposited on top of the rocks of the Gejiu Formation (Chen et al., 1992b).

The oldest magmatic rocks exposed in the Gejiu ore district are Middle Triassic basalts, whereas the most voluminous magmatic rocks are Late-Cretaceous intrusive rocks, ranging from gabbros to syenites and granitoids (Supplementary Material 1). To the east of the Gejiu Fault, the Late-Cretaceous magmatic rocks are equigranular and porphyritic granites. Most of the granites are not exposed and reach to a depth of 200 to 1000 m below the surface. There are, however, small outcrops of the Baishachong equigranular granite and the Beipaotai porphyritic granite to the north of the Malage deposit (Fig. 1c). The granitic bodies of Malage-Songshujiao (porphyritic granite), Laochang (porphyritic granite), and Laochang-Kafang (equigranular granite) have associated Sn deposits, i.e., the Malage Sn-Cu deposit, the Songshujiao Sn-Cu-Pb deposit, the Gaosong Sn-Pb-Zn deposit, the Laochang Sn-W-Cu deposit, and the Kafang Sn-Cu deposit (Fig. 1c). The porphyritic granites are mainly composed of K-feldspar (~33 %), plagioclase (~31 %), quartz (~26 %), and biotite (~8 %), with accessory contributions of zircon, apatite, titanite, ilmenite, allanite, magnetite, and/or monazite (Cheng and Mao, 2010). The equigranular granites mainly consist of microcline (~40 %), plagioclase (~25 %), quartz (~30 %), and biotite (~3 %) with accessory zircon, apatite, titanite, ilmenite, magnetite, monazite, tourmaline, and/or fluorite (Cheng and Mao, 2010).

To the west of the Gejiu Fault, magmatic rocks include gabbro,

syenite, and various granitoids, which are well exposed. Granitic rocks are dominated by the Longchahe porphyritic granitic and Shenxianshui equigranular granitic bodies (Fig. 1c). The outcrop area of the Longchahe granitic body, which is the largest intrusion in the Gejiu district, is about 200 km^2. The Longchahe granite mainly consists of microcline (~33 %), plagioclase (~31 %), quartz (~26 %), biotite (~8 %) and amphibole (~1 %) with accessory zircon, apatite, titanite, allanite, and magnetite (Guo, 2019). The Shenxianshui granitic body is medium to coarse grained with microcline (~35 %), plagioclase (~25 %), quartz (~30 %), and biotite (~3 %) and the accessory minerals zircon, apatite, titanite, tourmaline, and magnetite (Zhang et al., 2011). In the Jiasha area, there is a granitic body with mafic microgranular enclaves (Fig. 1c). This granite is mainly composed of plagioclase, K-feldspar, biotite, amphibole, and quartz with minor apatite, zircon, titanite, and magnetite (Zhang et al., 2013). The mafic microgranular enclaves contain plagioclase, hornblende, biotite, K-feldspar, and quartz, with rare titanite, zircon, magnetite, and apatite (Cheng et al., 2012a). To the west of the Gejiu Fault there is also gabbro and syenite. The gabbro consists of pyroxene, plagioclase, amphibole, and biotite with rare zircon, titanite, magnetite, and apatite (Cheng et al., 2012a). Syenite, which mainly outcrops in the Baiyunshan area (Fig. 1c), is fine to medium grained and consists of nepheline, K-feldspar, albite, Ti-rich andradite (melanite), biotite, aegirine-augite, and sodalite and the accessory minerals fluorite, titanite, zircon, ilmenite, rutile, and allanite (Cheng et al., 2013b).

(iii) Primary granite-related mineralization. To the east of the Gejiu Fault, there are five major deposits, i.e., the Malage (Sn-Cu), the Songshujiao (Sn-Cu-Pb), the Gaosong (Sn-Pb-Zn), the Laochang (Sn-W-Cu), and the Kafang (Sn-Cu) deposits, which are hosted by granite and their carbonate wall rocks. At the contact zone between the granite and carbonate wall rocks, there occur skarn-type Sn − Cu ± W mineralization with scheelite, chalcopyrite, arsenopyrite, bismuthinite, and cassiterite (Cheng et al., 2013a). In the carbonate wall rocks at some distance from the contact of the intrusion, there occur stratiform Sn − Pb ± Zn ± Cu ores (Cheng et al., 2013a; Zhang et al., 2020). The mineralization consists of pyrrhotite, cassiterite, pyrite, hematite, limonite, goethite, malachite, conichalcite, anglesite, cerusite, plumbojarosite, arsenopyrite, chalcopyrite, sphalerite, Fe-rich sphelarite, and galena with variable amounts of quartz, tourmaline, tremolite, and fluorite. Some ores hosted in the carbonates have complex shapes including lenticular, irregularly banded, and veined bodies that are directly related to faults (Jiang et al., 1997). Skarn and carbonate-hosted stratiform ores are the most important mineralization types and occur in all major sediment-hosted deposits. Apart from that, there is Sn-Cu mineralization within the Laochang-Kafang granite (Xu et al., 2021). The granite is variably altered and ore minerals including chalcopyrite and stannite occur in the most strongly altered sections of the granite, especially in steeply plunging veins. In the Laochang deposit, tourmaline veins with Sn − Be − W mineralization occur in the carbonate wall rocks above cupolas of unexposed granite (Cheng et al., 2012b). Metal zoning is well developed in the ore district with a change from Sn + Cu to Sn + Pb and to Pb + Zn mineralization from the granite to the carbonate wall-rocks (Jiang et al., 1997). Syntectonic mineralization occurred along dilatational jogs utilized by E-W oriented dextral faults (Jiang et al., 1997) indicating NW-SE directed regional compression with a dextral Ailaoshan Fault and a sinistral Gejiu Fault in the Late Cretaceous.

To the west of the Gejiu Fault, mineralization is sporadically distributed and deposits are generally only very small. The dominant ore elements in mineralization to the west of the Gejiu Fault are Pb and Sn. Ore bodies are mainly hosted in the wall rocks and the highest concentrations of ore elements are associated with the E-W and NNE-SSW striking faults (Zhang et al., 2015; Lu and Liu, 2020). Most ore bodies have been strongly weathered or oxidized. Because of their smaller size, mineralization to the west of the Gejiu Fault has been relatively little studied. There are only three deposits that have been mined (Lu and Liu, 2020; Fig. 1c): (i) the Douyan Sn-Pb deposit consists of strongly oxidized ore bodies hosted in carbonate rocks of the Gejiu Formation at the contact to the Ailaoshan Fault Zone; (ii) the Mengzong Pb deposit, consisting of strongly oxidized ore bodies with galena, cerussite, anglesite, and mimetite, is hosted in interlayer fracture zones on the surface of tuff and marlstone of the Falang Formation to the south of the Longchahe intrusion; and (iii) the Xiazhichang Pb deposit with complex lenticular ore bodies and irregular veins, in particular along E-W striking faults, is hosted in brecciated limestones and platy limestones of the Gejiu Formation.

3. Samples and methods

3.1. Samples

Granitoids to both sides of the Gejiu Fault have been sampled to expand the published data base. To the east of the Gejiu Fault, eight samples of the Laochang-Kafang granitic body were collected from the Zhuyeshan tunnel in the Laochang ore field. To the west of the Gejiu Fault, we collected five samples from the Shenxianshui granitic body, two samples from the Jiasha granitic body, and three samples from the Longchahe granitic body. One sample from each granitic rock was used for zircon analysis. Two samples from the Zhuyeshan granite and one sample each from the Shenxianshui, Jiasha, and Longchahe granitic rocks were used for apatite analysis.

3.2. Whole-rock chemical analysis

Granitic rock samples were washed and weathered surfaces were removed. The fresh portions of the samples were crushed and ground to less than 200 mesh. Whole rock major and trace element contents were determined at the Geochemistry Lab of China University of Geosciences, Beijing. Major element contents were determined using inductively coupled plasma-optical emission spectroscopy (Leeman Prodigy ICP-OES). Reference materials AGV-2, GSR-3, GSR-1, and GSR-5 were used as standards. Trace element contents were determined using inductively coupled plasma-mass spectrometry (Agilent-7500a ICP-MS). The standards AGV-2, BHVO-2, W-2 (U.S. Geological Survey), and GSR-3, GSR-1, and GSR-5 (National Geological Standard Reference Materials of China) were used to monitor the analytical accuracy. The analytical uncertainty is less than 5% for most trace elements, except less than 15% for P, K, and less than 10% for Cr, Sc, Cu, Zn, and Sr. Detailed procedures of major and trace element analysis are given by Zhong (2015).

3.3. Whole-rock Nd isotope analysis

Neodymium was separated and purified at the Key Laboratory of Orogenic Belts and Crustal Evolution, Peking University. Whole rock powders were dissolved in a mixture of HNO_3 + HF for seven days at 80℃ on the hot plate. REEs were separated on cation exchange columns filled with AG50W-X8 200 mesh resin. Neodymium was separated from the other REEs using a second cation-exchange column filled with P507 200 mesh resin. The Nd isotopic composition was determined on a Thermo-Finnigan TRITON thermal ionization mass spectrometer at the Tianjin Institute of Geology and Mineral Resources, China Geological Survey. Neodymium reference material LIRG gave $^{143}Nd/^{144}Nd = 0.512202 \pm 6$ (2σ, n = 3).

3.4. U-Pb dating, trace element analysis, and Hf-O isotope analysis of zircon

Zircon grains were separated using heavy liquids and magnetic methods and purified by handpicking under a binocular microscope. Zircon grains were mounted in an epoxy block and polished to expose the central sections of the crystals. The zircon grains were examined under transmitted and reflected light. Cathodoluminescence images were used to select domains for in situ elemental and isotopic analysis.

Zircon U-Pb dating and trace element analysis were conducted at Mineral and Fluid Inclusion Microanalysis Lab, Geology Institute, Chinese Academy of Geological Sciences in Beijing, using an Agilent 7900 ICP-MS coupled with an NWR 193UC laser ablation system (LA-ICP-MS). The analyses were performed using 30 μm spot diameter, 5 Hz repetition rate, and 2 J/cm^2 laser fluence. Zircon 91,500 was used as primary reference material and GJ-1 and Plešovice zircon were used as secondary reference materials. NIST 610 and ^{91}Zr were used as external reference material and internal standard element, respectively, to calibrate trace element contents. Data reduction was conducted using the Iolite software package (Paton et al., 2010) and weighted mean ^{206}Pb/^{238}U ages were calculated using the Isoplot program (Ludwig, 2003).

In situ zircon Hf isotope analysis was conducted at the National Research Center of Geoanalysis (Beijing) using a MC-ICP-MS (Neptune Plus, Thermo Fisher Scientific) coupled with a femto-second ($\lambda = 343$ nm) laser ablation system (J-200, Applied Spectra). The laser was operated at ~ 7 J/cm^2 fluence and 10 Hz repetition rate. The analyzed areas were approximately 40 × 20 μm. Detailed analytical procedures and data reduction procedures are given in Zhou et al. (2018).

In situ zircon O isotope analysis was conducted using a Cameca IMS 1280-HR at the SIMS Laboratory of Guangzhou Institute of Geochemistry, Chinese Academy of Sciences (GIGCAS). The analyses were performed using 10 kV acceleration voltage, 2nA beam current, and 10 μm beam diameter. Two reference zircon samples 91,500 and TEMORA 2, used to evaluate the reproducibility and accuracy, gave values consistent within error with the recommended values. The Penglai zircon was used as an external reference material to calibrate instrumental mass fractionation. Detailed analytical procedures and data reduction procedures are given in Yang et al. (2018).

3.5. Major and trace element analysis of apatite

Apatite major element contents were determined by electron microprobe using a JEOL-JXA8230 at the Institute of Mineral Resources, Chinese Academy of Geological Sciences (CAGS), Beijing, China. The minerals were analyzed using 15 kV accelerating voltage, 20nA beam current, and 5 μm spot diameter. The analytical error are less than 0.5 % for most elements.

Apatite trace element contents were measured using LA-ICP-MS at the In situ Mineral Geochemistry Lab, Ore Deposit and Exploration Centre (ODEC), Hefei University of Technology, China. The analyses were carried out on an Agilent 7900 Quadrupole ICP-MS coupled to a Photon Machines Analyte HE 193-nm ArF Excimer Laser Ablation system, using ~ 4 J/cm^2 fluence, 8 Hz repetition rate, and 30 μm spot diameter. Each analysis involved measuring the gas blank for 20 s and the sample for 40 s. Ca was used as internal standard and NIST 610, NIST 612, and BCR 2G were used as external standard materials. Standard reference materials were run after each 10 unknowns. Detection limits were calculated for each element and each spot analysis. Off-line data processing was performed using ICPMSDataCal (Liu et al., 2008). Analytical uncertainties were generally less than 10 % for most of the trace elements.

4. Results

4.1. Whole-rock chemical data

Major and trace element compositions of the Zhuyeshan (to the east of the Gejiu Fault) and Shenxianshui, Jiasha, and Longchahe (to the west of the Gejiu Fault) granitic rock samples are presented in Table 1.

Samples from the Zhuyeshan and Shenxianshui granites have similar chemical compositions although they come from opposite sides of the Gejju Fault. The Zhuyeshan and Shenxianshui granites are characterized by high contents of SiO_2 (71.2 to 75.7 wt%) and low contents of TiO_2 (0.13 to 0.30 wt%), TFe_2O_3 (1.24 to 2.80 wt%), MgO (0.15 to 0.59 wt%), CaO (0.49 to 1.65 wt%), and P_2O_5 (0.012 to 0.185 wt%). The contents of TFe_2O_3, MgO, CaO, and P_2O_5 show relatively small variations (Fig. 2b-e). The granitic rocks from Zhuyeshan to Shenxianshui show a decrease of Al_2O_3 (14.4 to 11.7 wt%) with increasing SiO_2 (Fig. 2a, g). Samples from these two granites have similar Na_2O and K_2O contents of 2.79 to 3.77 wt% and 4.16 to 5.69 wt%, respectively, plot in the granite field in the SiO_2 vs. $Na_2O + K_2O$ diagram (Fig. 3a), and belong to the high-K calc-alkaline series (Fig. 3b). Compared with the Zhuyeshan and Shenxianshui granites, the Jiasha and Longchahe granitoids have lower contents of SiO_2 (62.6 to 70.0 wt%) and higher contents of TiO_2 (0.43 to 0.97 wt%), TFe_2O_3 (2.79 to 5.74 wt%), MgO (0.81 to 2.07 wt%), CaO (1.58 to 4.06 wt%), P_2O_5 (0.182 to 0.418 wt%), and Al_2O_3 (14.2 to 17.2 wt%; Fig. 2a-e and g). In addition, the Jiasha granitoid have higher SiO_2 and lower TFe_2O_3, MgO, CaO, and P_2O_5 than the Longchahe granitoid (Fig. 2a-e). Samples from the Jiasha and Longchahe granitoids show similar Na_2O (3.14–3.70 wt%) and K_2O (4.33–6.10 wt%) contents as the Zhuyeshan and Shenxianshui granites (Fig. 2h, i), most samples plot in the quartz monzonite field in the SiO_2 vs. $Na_2O + K_2O$ diagram (Fig. 3a), and belong to the shoshonitic series (Fig. 3b).

Fig. 4 shows trace element pattern (normalized to upper continental crust, UCC; Rudnick and Gao, 2003) of the samples from the Zhuyeshan, Shenxianshui, Jiasha, and Longchahe granitoids. There are two types of pattern, i.e., the Zhuyeshan and Shenxianshui granitic rocks have similar pattern that differ significantly from those of the Jiasha and Longchahe granitic rocks. The Zhuyeshan granite samples are characterized by flat REE pattern, a deep Eu anomaly, and a pronounced tetrade effect. Apart from Eu, the pattern show marked depletions in V, Cr, Co, Ni, Sr, and Ba, and distinct peaks for Li, Rb, Nb, Sn, Cs, Ta, Pb, Th, and U. Samples from the Shenxianshui granite also show a tetrade effect, but show slightly higher LREE and Li enrichment, more variable negative Eu anomalies, and stronger depletions of Sc, V, Cr, Co, and Ni than samples from the Zhuyeshan granite. In comparison with these two granites, the samples from the Jiasha and Longchahe intrusions show a strong LREE enrichment and only slightly negative Eu anomalies (Jiasha) or no Eu anomalies (Longchahe). Furthermore, the Jiasha and Longchahe granitoids show higher contents for Ba, Sr, Sc, V, Cr, Co, Ni, Zn, Zr, and Hf and lower contents of Rb, Cs, Ta, and U than samples from the Zhuyeshan and Shenxianshui granites. We estimated the melting temperatures of the granitic melts using the zircon saturation thermometer of Watson and Harrison (1983). The Zr contents of the samples from the Zhuyeshan, Shenxianshui, Jiasha, and Longchahe granitoids are 112–226 ppm, 189–230 ppm, 242–263 ppm, and 292–399 ppm, respectively (Table 1), the corresponding zircon saturation temperatures are 760–823 ℃, 785–813 ℃, 813–830 ℃, and 802–831 ℃, respectively.

4.2. Whole rock Nd isotopic composition

Measured and initial whole-rock Nd isotopic compositions are presented in Table 2. The initial isotopic compositions of Nd was calculated for an U-Pb zircon age of 83 Ma. The εNd(t) values of the Zhuyeshan granite range from − 9.0 to − 8.3. The εNd(t) values of granitoids to the west of the Gejiu Fault are slightly higher than those of the Zhuyeshan granite, ranging from − 7.3 to − 7.0 (Shenxianshui), −7.8 to − 7.7 (Jiasha), and − 7.6 to − 7.1 (Longchahe), respectively. The corresponding two-stage model ages (Liew and Hofmann, 1988) are 1564 to 1506 Ma (Zhuyeshan), 1424 to 1401 Ma (Shenxianshui), 1466 to 1459 Ma (Jiasha), and 1450 to 1412 Ma (Longchahe), respectively. Note, two-stage model ages are preferred here, as the more evolved granites show a tetrade effect and, thus, their REE pattern strongly differ from the ones of the protolith of the granites, typically yielding incorrect single-stage model ages.

4.3. Zircon U-Pb ages, trace element, and Hf-O isotopic compositions

The results of zircon U-Pb dating, trace element analysis, and Hf and O isotope analysis are presented in the Supplementary Material 2. Zircon

Table 1
Whole rock major (in wt.%) and trace elements (in ppm) data of the Zhuyeshan (ZYS), Shenxianshui (SXS), Jiasha (JS), and Longchahe (LCH) granitoids from the Gejiu district, China.

Sample no.	To the east of the Gejiu Fault								To the west of the Gejiu Fault									
	ZYS-16	ZYS-26	ZYS-27	ZYS-28	ZYS-29	ZYS-30	ZYS-31	ZYS-32	SXS-4	SXS-5	SXS-6	SXS-7	SXS-9	JS-1	JS-2	LCH-2	LCH-4	LCH-7
SiO_2	75.1	74.0	72.9	71.2	74.4	72.1	71.9	72.0	74.4	75.5	75.2	75.7	74.6	64.7	70.0	63.8	62.6	62.6
TiO_2	0.14	0.20	0.23	0.30	0.26	0.27	0.26	0.29	0.17	0.16	0.15	0.13	0.14	0.45	0.43	0.70	0.97	0.82
Al_2O_3	12.6	12.7	14.2	14.3	13.1	14.4	14.4	14.2	12.4	11.8	11.9	11.7	12.3	17.2	14.2	15.9	15.2	16.7
TFe_2O_3	1.46	1.58	1.86	2.80	2.05	2.22	2.16	2.26	1.51	1.42	1.40	1.24	1.29	3.07	2.79	4.11	5.74	5.04
MnO	0.035	0.037	0.043	0.085	0.043	0.048	0.047	0.053	0.044	0.037	0.028	0.042	0.046	0.059	0.056	0.069	0.093	0.083
MgO	0.30	0.32	0.41	0.59	0.47	0.50	0.48	0.51	0.24	0.19	0.23	0.15	0.18	0.88	0.81	1.48	2.07	1.82
CaO	0.79	0.97	1.05	1.65	1.06	1.13	1.26	1.25	0.89	0.49	0.61	0.63	0.87	1.83	1.58	3.37	4.06	3.94
Na_2O	3.21	2.79	3.10	3.09	3.04	3.27	3.10	3.28	3.46	3.04	3.26	3.34	3.77	3.70	3.14	3.36	3.33	3.37
K_2O	4.92	5.69	4.86	4.40	4.16	4.69	4.61	4.66	5.26	5.35	5.55	5.25	5.29	6.10	4.95	5.93	4.64	4.33
P_2O_5	0.131	0.109	0.166	0.170	0.154	0.184	0.185	0.178	0.048	0.032	0.037	0.012	0.031	0.231	0.182	0.303	0.418	0.353
Lol	0.76	1.04	0.74	1.01	0.69	0.79	1.16	0.92	0.48	0.85	0.61	0.67	0.43	1.16	1.05	0.33	0.24	0.40
Total	99.4	99.5	99.5	99.6	99.4	99.6	99.6	99.6	99.0	98.9	98.9	98.9	99.0	99.4	99.1	99.3	99.3	99.4
Li	42	76	83	83	96	96	93	108	140	134	118	131	277	78	89	64	93	77
Sc	3.7	3.4	3.6	6.3	3.6	4.1	4.1	4.2	1.7	1.6	1.7	1.2	1.4	4.8	4.7	6.4	7.9	7.3
V	7.0	8.9	10	16	12	13	13	13	8.2	8.0	8.2	5.3	5.9	31	31	63	84	71
Cr	3.1	7.1	4.6	7.9	5.4	4.1	4.6	7.4	1.6	3.2	2.6	1.5	8.6	11	11	23	27	23
Co	1.4	2.1	2.2	3.1	2.4	3.0	2.7	2.6	1.2	1.1	1.2	0.9	1.0	5.0	3.9	9.6	12.9	10.6
Ni	1.2	4.1	2.1	3.3	2.7	1.9	1.9	4.0	0.7	1.7	1.5	0.6	2.4	3.8	4.3	8.2	9.7	7.7
Cu	9.89	118	2.06	2.65	1.84	2.62	47.6	4.19	17.9	35.3	2.34	2.32	2.81	6.57	11.8	7.63	13.4	11.7
Zn	43	73	60	68	61	66	79	72	81	61	49	37	38	93	63	107	142	127
Ga	17.6	21.4	21.0	21.7	20.4	22.9	22.2	22.5	20.6	21.6	19.7	20.7	22.7	25.4	26.4	25.9	29.7	26.5
Rb	395	436	392	407	372	409	418	423	428	458	466	474	528	289	302	248	242	220
Sr	205	108	96	181	101	97	118	96	226	200	178	135	130	361	329	760	699	672
Y	26.1	26.1	24.2	42.1	21.1	23.6	25.2	26.4	27.5	47.6	16.1	18.7	18.0	19.1	20.1	22.4	30.5	27.7
Zr	112	153	157	226	175	159	177	197	230	198	197	189	180	242	263	292	399	359
Nb	28.8	31.6	29.3	51.7	28.3	33.9	32.2	33.0	48.3	49.2	44.2	45.8	48.2	26.0	27.7	24.1	32.7	27.6
Sn	6.36	10.5	11.6	3.63	10.3	14.2	7.15	11.5	n.a.	n.a.	n.a.	n.a.	n.a.	n.a.	n.a.	n.a.	n.a.	n.a.
Cs	20.0	45.3	39.5	25.0	34.5	41.1	43.0	40.6	19.2	22.8	15.6	21.4	40.2	11.7	13.1	8.2	9.4	7.8
Ba	169	167	212	504	229	210	230	230	279	304	292	238	237	873	677	1766	1240	1132
La	36.8	43.8	54.4	67.6	55.1	55.1	59.2	64.6	78.4	75.5	70.5	69.2	61.6	110	106	125	160	155
Ce	81.1	94.3	110	132	111	111	121	128	141	103	121	114	110	201	188	233	305	290
Pr	8.89	10.07	11.57	14.24	11.71	11.71	12.67	13.67	12.33	13.16	11.47	10.84	9.77	19.04	18.18	22.64	30.14	27.80
Nd	32.3	35.3	40.7	51.4	41.1	41.3	44.5	48.0	37.8	42.9	36.1	33.3	29.3	61.4	59.2	75.6	99.8	92.1
Sm	7.41	7.29	7.97	11.1	7.83	8.00	8.70	9.24	6.05	8.35	5.65	5.65	4.52	9.37	9.12	11.6	15.14	13.91
Eu	0.44	0.36	0.48	0.87	0.52	0.50	0.51	0.51	0.74	1.23	0.66	0.56	0.52	1.46	1.35	2.51	2.74	2.52
Gd	6.52	5.97	6.39	9.71	6.10	6.31	6.82	7.24	4.86	7.57	4.09	4.39	3.35	6.52	6.48	8.16	10.5	9.72
Tb	0.95	0.85	0.84	1.39	0.78	0.84	0.89	0.94	0.65	1.14	0.51	0.59	0.42	0.73	0.74	0.90	1.15	1.08
Dy	5.48	5.06	4.86	8.34	4.39	4.78	5.10	5.40	3.81	6.84	2.84	3.36	2.30	3.69	3.85	4.59	5.84	5.50
Ho	1.0	0.9	0.9	1.5	0.8	0.9	0.9	1.0	0.8	1.3	0.5	0.6	0.5	0.6	0.7	0.8	1.0	0.9
Er	2.62	2.72	2.51	4.41	2.19	2.43	2.58	2.73	2.25	3.87	1.55	1.74	1.37	1.68	1.76	1.99	2.57	2.41
Tm	0.4	0.4	0.4	0.7	0.3	0.4	0.4	0.4	0.4	0.6	0.3	0.3	0.2	0.2	0.3	0.3	0.4	0.3
Yb	2.49	2.78	2.46	4.29	2.08	2.37	2.51	2.66	2.49	4.35	1.79	1.78	1.61	1.46	1.57	1.61	2.06	1.93
Lu	0.4	0.4	0.4	0.6	0.3	0.3	0.4	0.4	0.4	0.7	0.3	0.3	0.3	0.2	0.2	0.2	0.3	0.3
Hf	3.23	3.92	3.87	5.56	4.14	3.90	4.28	4.69	5.60	4.99	5.15	4.49	4.39	5.79	6.36	6.58	9.32	8.63
Ta	1.87	2.37	2.00	3.70	1.88	2.51	2.50	2.05	3.10	3.13	2.77	2.73	2.96	1.46	1.59	1.38	1.79	1.61
Pb	54.5	61.6	54.0	42.3	50.0	53.5	57.3	56.1	44.5	49.1	44.0	57.5	56.4	35.56	37.7	42.2	30.54	32.64
Th	39.8	39.5	47.2	44.1	47.1	49.1	52.4	57.8	69.7	59.0	68.0	61.8	57.5	64.3	68.6	44.3	58.3	56.0
U	18.8	19.5	15.8	15.5	12.8	19.1	19.4	16.4	17.3	20.7	17.2	17.7	11.7	9.9	9.0	5.0	5.5	5.6
Rb/Sr	1.93	4.05	4.07	2.25	3.70	4.23	3.55	4.42	1.89	2.29	2.61	3.51	4.06	0.80	0.92	0.33	0.35	0.33
T (°C)*	760	782	795	823	807	795	806	812	813	808	800	797	785	813	830	802	823	831

* Temperatures were calculated using the Watson and Harrison (1983) zircon saturation thermometer.

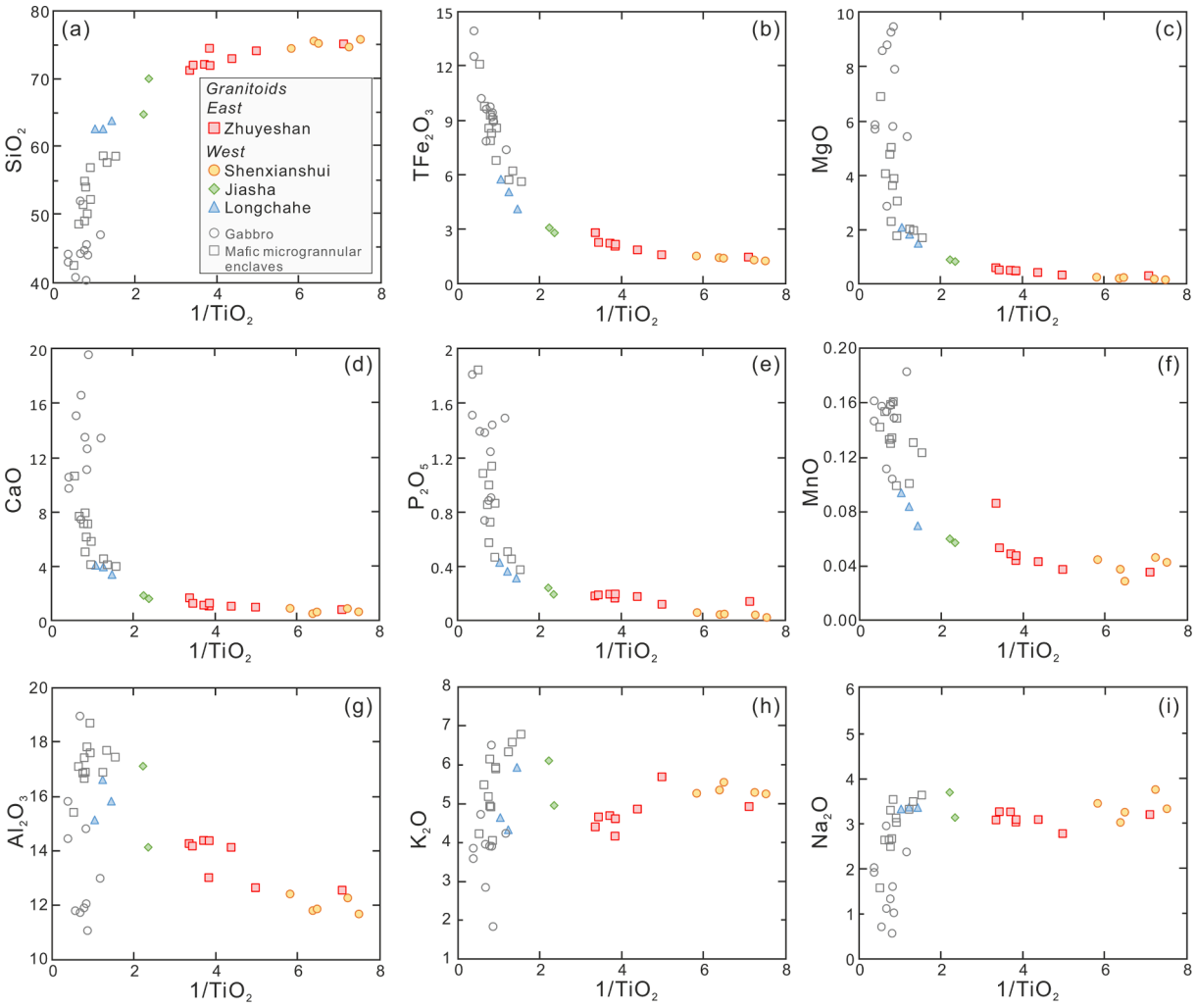

Fig. 2. Major elements vs. $1/TiO_2$ diagrams for granitoids intruded to the east and west of the Gejiu Fault. $1/TiO_2$ increases with magma evolution. The Zhuyeshan and Shenxianshui granites are characterized by high contents of SiO_2 and low contents of TiO_2, TFe_2O_3, MgO, CaO, and P_2O_5. These two types of granites show – with stronger fractionation – an increase in SiO_2, decrease in Al_2O_3, but small variations in TFe_2O_3, MgO, CaO, and P_2O_5. Compared with the Zhuyeshan and Shenxianshui granites, the Jiasha and Longchahe granitoids have lower contents of SiO_2 and higher contents of TiO_2, TFe_2O_3, MgO, CaO, P_2O_5, and Al_2O_3. Furthermore, samples from the Jiasha granitoid have higher SiO_2 and lower TFe_2O_3, MgO, CaO, and P_2O_5 contents than those from the Longchahe granitoid. The four types of granitoids have similar contents of K_2O and Na_2O. Data for mafic microgranular enclaves and gabbros are from Cheng et al. (2013b).

crystals from the granitoids are enhedral and cathodoluminescence images typically show magmatic oscillatory zoning, which indicates that the zircon crystals have a magmatic origin. Measured Th/U ratios generally fall in the range from 0.2 to 1.7 (Supplementary Material 2). The weighted mean $^{206}Pb/^{238}U$ ages of the granitoids are 82.94 ± 0.48 Ma (Zhuyeshan), 82.52 ± 0.62 Ma (Shenxianshui), 82.81 ± 0.58 Ma (Jiasha), and 83.08 ± 0.52 Ma (Longchahe), respectively (Fig. 5). These ages indicate that the granitic rocks distributed to both sides of the Gejiu Fault were emplaced at the same time.

The zircon Eu anomaly (Eu/Eu*) of the Zhuyeshan, Shenxianshui, and Jiasha granitoids generally fall in the same range (0.01 to 0.31), whereas the Longchahe granitoid generally have higher Eu/Eu* ratios (0.19–0.42; Fig. 6a). All four types of the granitoids have similar zircon Ce/Ce* anomalies (3–219; Fig. 6a) and calculated Ti-in-zircon temperatures (674–905 °C; Ferry and Watson, 2007). The magma oxygen fugacity (fO_2) was calculated using zircon trace element data (Loucks et al., 2020). The granitoids have similar calculated logfO_2 values that correspond to ΔFMQ values ranging from − 2.19 to 2.67, with most values being less than zero (Fig. 6b).

The Hf isotopic compositions of the dated zircon grains correspond to calculated εHf(t) values ranging from − 8.2 to − 5.9 (Zhuyeshan), −6.6 to − 2.7 (Shenxianshui), −7.8 to − 4.9 (Jiasha), and − 7.8 to − 4.0 (Longchahe). These εHf(t) values corresponded to T_{DM2} ages ranging from 1676 to 1522 Ma (Zhuyeshan), 1566 to 1409 Ma (Shenxianshui with one younger model age at 1318 Ma), 1640 to 1457 Ma (Jiasha), and 1643 to 1408 Ma (Longchahe). Although the data for the various granitoids fall in relatively narrow, overlapping clusters, a few analyses from the Shenxianshui granite yield slightly higher εHf(t) values (Fig. 7a). The $\delta^{18}O$ values of the Zhuyeshan, Shenxianshui, Jiasha, and Longchahe granitic rocks range from 7.30 to 8.95 ‰, 9.12 to 10.28 ‰, 8.16 to 9.12 ‰, and 7.99 to 9.32 ‰, respectively. Most samples have $\delta^{18}O$ values in the range from 8 to 9 ‰, but some samples from the Shenxianshui granite have slightly higher $\delta^{18}O$ values and two samples from Zhuyeshan granite have lower $\delta^{18}O$ values (Fig. 7a).

4.4. Apatite major and trace element compositions

Major and trace element compositions of apatite from the Zhuyeshan, Shenxianshui, Jiasha, and Longchahe granitic rocks are presented in Supplementary Material 3. The CaO, P_2O_5, and SiO_2 contents of apatite range from 52.5 to 57.0 wt%, 36.5 to 43.0 wt%, and from below the detection limit to 0.64 wt%, respectively. Apatite from the Zhuyeshan granite has relatively large ranges of MnO (up to 1.07 wt%) and FeO (up to 0.52 wt%) contents, whereas the corresponding ranges for

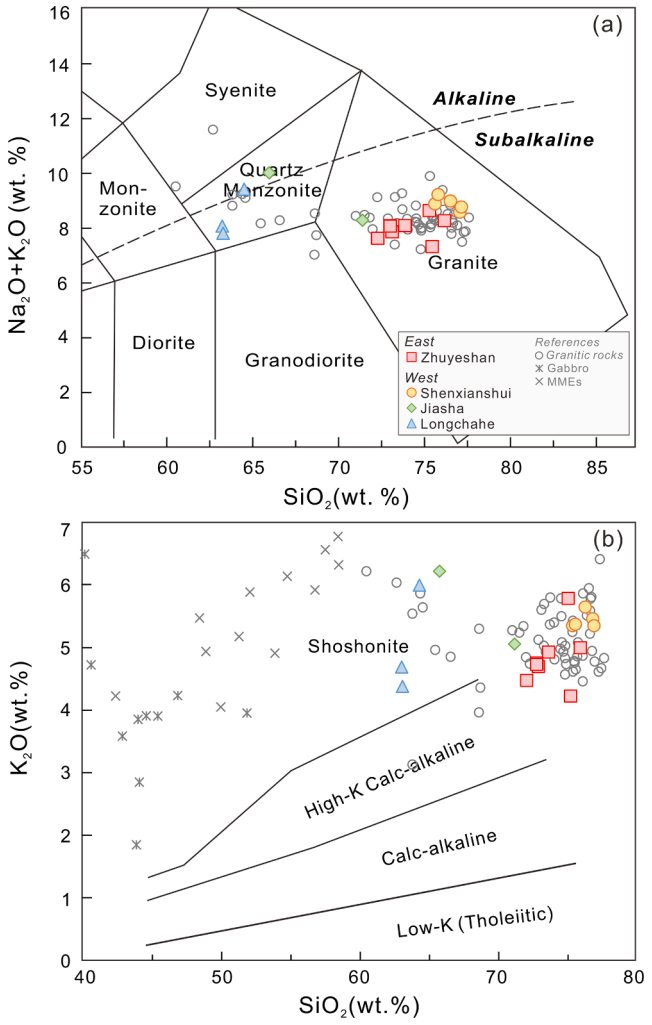

Fig. 3. Classification of granitoids in the (a) SiO_2 vs. $Na_2O + K_2O$ and (b) SiO_2 vs. K_2O diagrams. Samples from the Zhuyeshan and Shenxianshui granites plot in the granite field and belong to the high-K calc-alkaline series, whereas samples from the Jiasha and Longchahe intrusions plot in the granite and quartz monzonite fields and belong to the shoshonitic series. Additional data for granitic rocks, mafic microgranular enclaves, and gabbros are from Cheng and Mao (2010) and Cheng et al. (2013b).

the Shenxianshui, Jiasha, and Longchahe granitic rocks are below 0.22 wt% MnO and below 0.10 wt% FeO. Apatite from all granitic rocks is enriched in F (2.34 to 5.42 wt%), whereas the content of SO_3 is below 0.47 wt%.

Fig. 8 shows the rare earth element pattern of apatite from the Zhuyeshan, Shenxianshui, Jiasha, and Longchahe granitoids. For the Zhuyeshan granite, apatite from whole rock sample ZYS-29 show flat REE pattern with deep negative Eu anomalies, weakly positive Ce anomalies, and slightly negative La anomalies, whereas apatite from whole rock sample ZYS-28 show LREE enrichment and HREE depletion. Apatite from the Zhuyeshan granite has low Sr (52 to 286 ppm) and high Y (1087 to 5291 ppm) contents (Fig. 9). In comparison with the Zhuyeshan granite, the patterns of apatite from the Shenxianshui, Jiasha, and Longchahe granitoids are similar to the pattern of apatite from the whole rock sample ZYS-28 that is characterized by LREE enrichment and HREE depletion with variably negative Eu anomalies. Apatite from the Shenxianshui granite has similar Sr and Y contents (130–373 ppm Sr, 317–3194 ppm Y) as those from the Zhuyeshan granite, whereas apatite from the Jiasha and Longchahe granitoids have higher Sr (177–641 ppm) and lower Y (196–675 ppm) contents (Fig. 9).

5. Discussion

5.1. Granite chemistry as proxy for Sn mineralization in the Gejiu area

(i) Age of magmatism. The weighted mean $^{206}Pb/^{238}U$ ages of the Zhuyeshan, Shenxianshui, Jiashan, and Longchahe granitoids are around 83 Ma (Fig. 5). Therefore, the Cretaceous granitoids to the east and west of the Gejiu Fault should have formed during the same tectonic event. The mineralization ages of the major deposits formed to the east of the Gejiu Fault were determined by mica ^{40}Ar-^{39}Ar dating (95 to 77 Ma, Cheng et al., 2013a), molybdenite Re-Os dating (86 to 83 Ma, Cheng et al., 2012b), and cassiterite U-Pb dating (85 to 84 Ma, Guo et al., 2018; 83 to 77 Ma, Cheng et al., 2019). To the west of the Gejiu Fault, gabbro, syenite, and mafic microgranular enclaves have zircon U-Pb ages of 83.3 Ma, 79.2 Ma, and 83.1 Ma, respectively (Cheng and Mao, 2010). Late Cretaceous magmatic rocks to the east and west sides of the Gejiu Fault and primary Sn mineralization in the Gejiu district formed at the same time.

(ii) Source rocks. The Zhuyeshan granite to the east of the Gejiu Fault and the Shenxianshu, Jiasha, and Longchahe granitoids to the west of the Gejiu Fault show a very narrow range of whole-rock Nd isotopic compositions, with εNd(t) values ranging from − 9.0 to − 7.0 (Table 2). The corresponding two-stage model ages (Liew and Hofmann, 1988) range from 1564 to 1401 Ma. Hafnium isotope data from magmatic zircon yield the same range of model ages as the whole rock Nd isotope data. The Mesoproterozoic model ages indicate significant contributions from old continental crust to the source of the granitoids.

The predominance of crustal source rocks is supported by zircon Hf and O isotope data. The εHf(t) and $\delta^{18}O$ values of most samples from the Zhuyeshan, Jiasha, and Longchahe granitoids fall in a narrow and overlapping cluster and show minor incorporation of mantle derived material (Fig. 7a). Data from the Shenxianshui granite in part have higher $\delta^{18}O$ values, which may indicate intense chemical weathering of the sedimentary protoliths. The whole rock Nd and the zircon Hf and O isotope data demonstrate that the granitoids to both sides of the Gejiu Fault are dominantly derived from metasedimentary rocks whose sources experienced intense chemical weathering before sedimentation and burial. Contributions of mantle-derived magma, locally preserved in mafic microgranular enclaves, are minor.

(iii) Melting conditions. Melting temperature is critical for Sn-enrichment in the melt: low temperature melting (muscovite dehydration melting) results in enrichment of Sn in restite minerals such as biotite, whereas high temperature melting (biotite dehydration melting) results in the partitioning of Sn into the melt (Romer and Kroner, 2016). This general relation is supported by case studies (Wolf et al., 2018; Yuan et al., 2019). The melting temperature of the granitic melts was estimated using the zircon saturation thermometer of Watson and Harrison (1983). Samples from the Zhuyeshan granite yield high zircon saturation temperatures (760 to 822 ℃; Table 1) that fall in a similar range as those of the Shenxianshui, Jiasha, and Longchahe granitoids to the west of the Gejiu Fault (785 to 831 ℃; Table 1). These temperature ranges are higher than temperatures typical for muscovite dehydration melting (~720–740 ℃; Viruete et al., 2000) and reach into the temperature range of biotite dehydration melting (>800 ℃; Barbero, 1995). The calculated temperatures are likely to represent minimum estimates of the melting temperature due to the absence of inherited zircon in the investigated samples from these granitoids (Miller et al., 2003). Thus, Cretaceous granitoids to both sides of the Gejiu Fault are derived from high-temperature melting of crustal protoliths. The calculated Ti-in-zircon temperatures show a large variation and are significantly lower than the calculated zircon saturation temperatures, possibly indicating that the Ti-in-zircon thermometer does not work reliably in highly evolved rocks with very low Ti contents.

High oxygen fugacity during partial melting of protoliths will stabilize Sn-sequestering phases such as biotite, rutile, and titanite, which in turn will result in the enrichment of Sn in the restite rather than in the

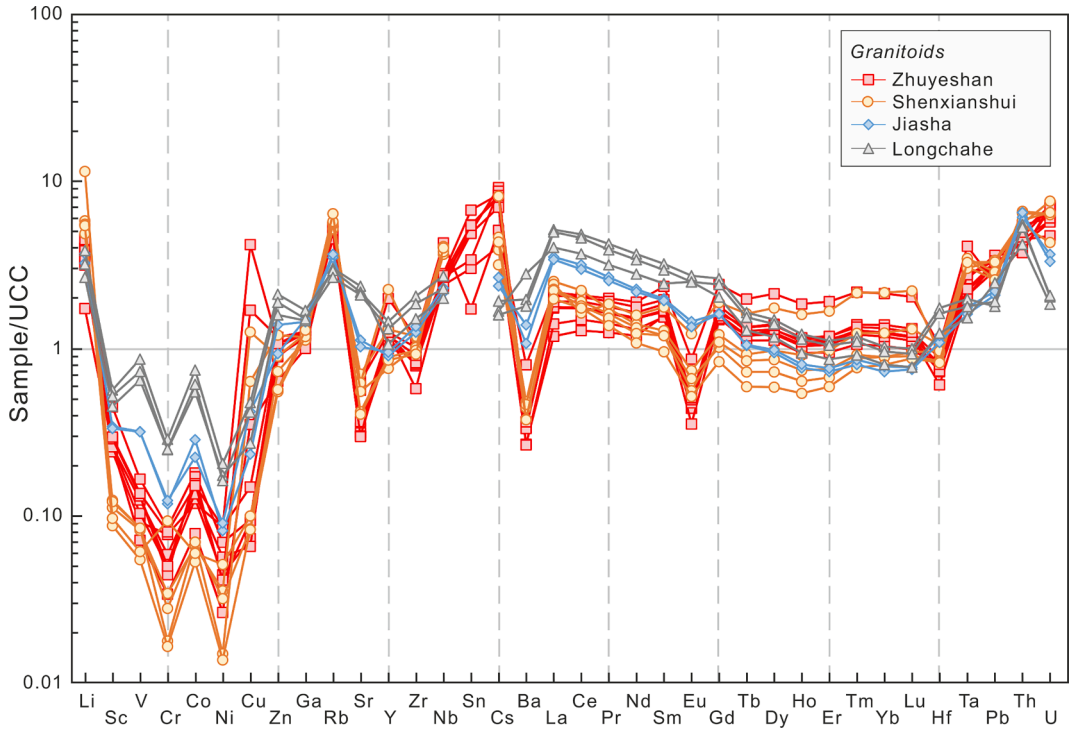

Fig. 4. Trace element pattern for the Zhuyeshan granite to the east of the Gejiu Fault and for the Shenxianshui, Jiasha, and Longchahe granitoids to the west of the Gejiu Fault, normalized to the Upper Continental Crust (UCC; Rudnick and Gao, 2003). The Zhuyeshan and Shenxianshui granites have similar patterns that are characterized by flat REE pattern, a deep Eu anomaly, and a pronounced tetrade effect. The patterns show marked depletions in V, Cr, Co, Ni, Sr, and Ba, and distinct peaks for Li, Rb, Nb, Sn, Cs, Ta, Pb, Th, and U. The patterns for the Jiasha and Longchahe granitoids are different from those of the Zhuyeshan and Shenxianshui granites, showing a strong LREE enrichment and only slightly negative Eu anomalies (Jiasha) or no Eu anomalies (Longchahe). Furthermore, the Jiasha and Longchahe granitoids show higher contents of Ba, Sr, Sc, V, Cr, Co, Ni, Zn, Zr, and Hf and lower contents of Rb, Cs, Ta, and U than the samples from the Zhuyeshan and Shenxianshui granites

Table 2
Nd isotopic compositions of the Zhuyeshan (ZYS), Shenxianshui (SXS), Jiasha (JS), and Longchahe (LCH) granitoids from the Gejiu district, China.

Sample no.	*t*(Ma)	Sm (ppm)	Nd (ppm)	$^{143}Nd/^{144}Nd$	2σ	$(^{143}Nd/^{144}Nd)_i$	$\varepsilon_{Nd}(t)$	T_{DM2} (Ma)
To the east of the Gejiu Fault								
ZYS-16	83	7.41	32.3	0.512155	0.000006	0.51208	−8.8	1546
ZYS-26	83	7.29	35.3	0.512136	0.000006	0.51207	−9.0	1564
ZYS-27	83	7.97	40.7	0.512147	0.000003	0.51208	−8.8	1542
ZYS-28	83	11.0	51.4	0.512176	0.000004	0.51211	−8.3	1506
ZYS-29	83	7.83	41.1	0.512142	0.000002	0.51208	−8.8	1547
ZYS-30	83	8.00	41.3	0.512141	0.000003	0.51208	−8.9	1550
ZYS-31	83	8.70	44.5	0.512134	0.000004	0.51207	−9.0	1561
ZYS-32	83	9.24	48.0	0.512137	0.000004	0.51207	−8.9	1555
To the west of the Gejiu Fault								
SXS-4	83	6.05	37.8	0.512212	0.000003	0.51216	−7.3	1424
SXS-5	83	8.35	42.9	0.512226	0.000005	0.51216	−7.2	1420
SXS-6	83	5.65	36.1	0.512218	0.000003	0.51217	−7.1	1413
SXS-7	83	5.65	33.3	0.512230	0.000005	0.51217	−7.0	1401
SXS-9	83	4.52	29.3	0.512215	0.000003	0.51216	−7.2	1417
JS-1	83	9.37	61.4	0.512182	0.000004	0.51213	−7.8	1466
JS-2	83	9.12	59.2	0.512187	0.000007	0.51214	−7.7	1459
LCH-2	83	11.57	75.6	0.512210	0.000006	0.51216	−7.2	1424
LCH-4	83	15.14	99.8	0.512216	0.000002	0.51217	−7.1	1414
LCH-7	83	13.91	92.1	0.512217	0.000005	0.51217	−7.1	1412

melt (Wolf et al., 2018). High oxygen fugacity furthermore favors the crystallization of magnetite and titanite, which may incorporate significant amounts of Sn, during fractional crystallization and, thus, prevent the enrichment of Sn in volatile-rich melts (Ishihara, 1979). The formation of Sn mineralization is favored by low oxygen fugacity during melting and fractional crystallization. The calculated zircon oxygen fugacity (expressed as ΔFMQ values) of the granitoids overlaps and corresponds to values that are generally more reduced than the FMQ (fayalite–magnetite–quartz) buffer, i.e., that are close or fall below FMQ (Fig. 6b). Thus, the granitic rocks to both sides of the Gejiu Fault have similarly low oxygen fugacity. This is supported by the same range of zircon Ce/Ce* values (Fig. 6a) that have been used to indicate the redox state of the magma (Burnham and Berry, 2012). In contrast, the relatively large variation in zircon Eu/Eu* values among the Cretaceous granitic rocks of the Gejiu area is likely to reflect different extents of magma fractionation (Gardiner et al., 2017).

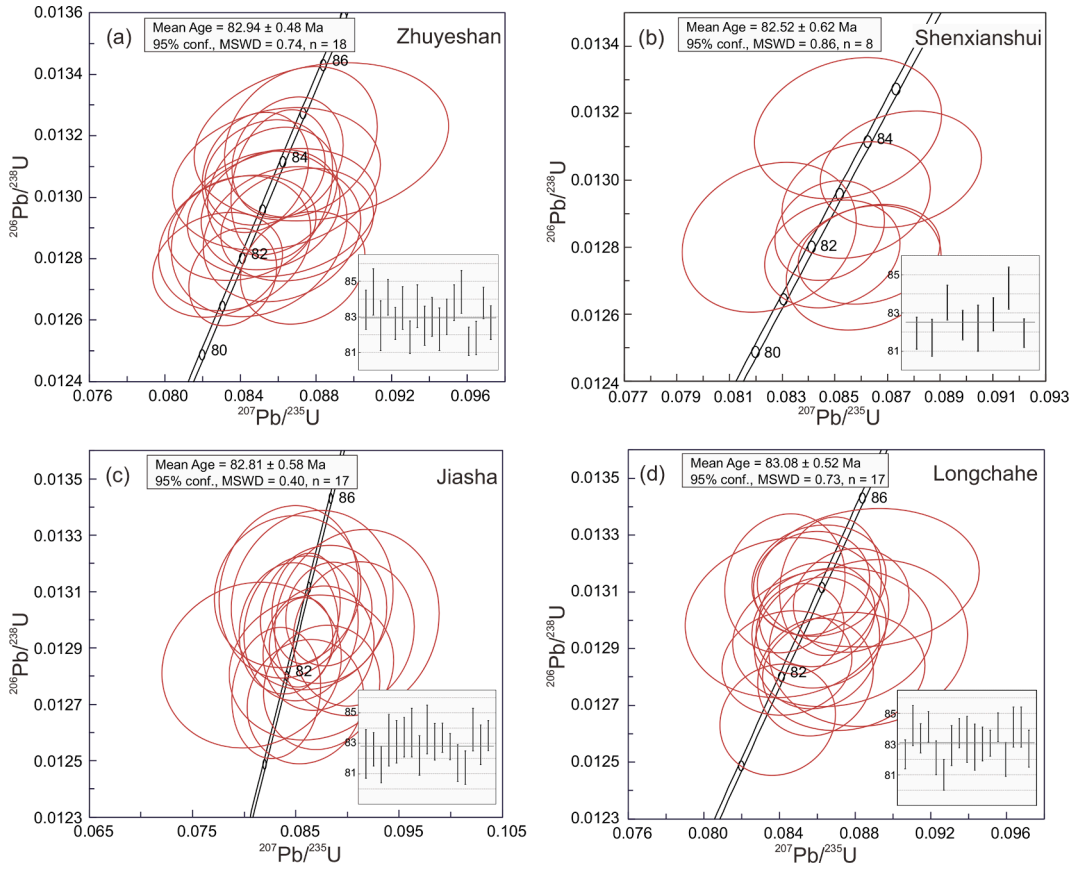

Fig. 5. Concordia diagrams for LA-ICP-MS zircon U-Pb data from the (a) Zhuyeshan, (b) Shenxianshui, (c) Jiasha, and (d) Longchahe granitoids.

(iv) Extent of fractionation. Sn mineralization generally is thought to be associated with highly fractionated granites that eventually concentrate Sn in the late-magmatic hydrothermal fluids. Both, the Zhuyeshan and the Shenxianshui granite have flat (or almost flat) UCC-normalized REE patterns with deep Eu anomalies, show variably pronounced tetrade effects, are markedly enriched in Li, Rb, Cs, Ta, Hf, and U, and are depleted in Sr, Ba, and Zr (Fig. 4). These chemical signatures are typical for highly evolved magmatic rocks. These signatures are not observed in samples from the Jiasha and Longchahe granitoids (Fig. 4). Whole-rock Rb/Sr ratios are commonly used to indicate the extent of magma fractionation. The Rb/Sr ratios of the Zhuyeshan and Shenxianshui granites have similar ranges (1.93–4.42 and 1.89–4.06, respectively) and are markedly higher than those of the Jiasha and Longchahe granitoids (0.33 to 0.92; Table 1). Therefore, the Jiasha and Longchahe granotoids are less evolved than the Zhuyeshan granite to the east of the Gejiu Fault and the Shenxianshui granite to the west of the Gejiu Fault, which have the composition of highly evolved tin granites (e.g., Olade, 1980; Xu et al., 2015). Rare earth elements of apatite from these granitoids generally show the same pattern characterized by LREE-enrichment and variably negative Eu anomalies that is typical for granitoids (Belousova et al., 2002; Fig. 8). Apatite from the whole rock sample ZYS-29 has higher HREE contents and higher Y contents than apatite from the other granites. Apatite from the Zhuyeshan and Shenxianshui granite has distinctly higher Y contents than apatite from the Jiasha and Longchahe granitoids and shows negative correlation between Y and Sr contents (Fig. 9), which is typical for highly fractionated granites (e.g., Belousova et al., 2002; Chu et al., 2009; Cao et al., 2013). Thus, Cretaceous fertile granites occur to the east and the west of the Gejiu Fault.

5.2. Similar type of magmatism and different mineralization potential to the east and west of the Gejiu Fault: A case for contrasting structural conditions of magma emplacement?

There are fertile tin granites to both sides of the Gejiu Fault. Therefore, the contrasting distribution of mineralization between the eastern and western sectors cannot be explained by the presence or absence of fertile tin granites. There are two unrelated alternative explanations for the poorly mineralized western sector: (i) different present-day exposure levels in the western and eastern sectors, implying that mineralization in the western sector may have been removed by erosion or is still at greater depths, whereas mineralization in the eastern sector is close to the present surface; (ii) different orientations of the stress field in the two sectors during the late magmatic processes leading to the formation of the Sn deposits. The spatial distribution of the deposits is structurally controlled by the conjugate fracture system of the Gejiu and Ailaoshan faults (Fig. 1a). For both possible explanations, these faults represent necessary first order structures either by permitting differential uplift and erosion or by separating domains of contrasting stress fields.

The deeper level of exposure in the western sector requires differential uplift of the western side along the Gejiu Fault as well as decoupling of both domains along the Ailaoshan Fault. Major erosion after the emplacement of the Cretaceous magmatic rocks would have removed potential Sn mineralization. In such a scenario, there is no essential difference in the formation of primary granite-related Sn deposits. Furthermore, the uplift of the western side and fault activity occurred after the formation of Sn mineralization. Different levels of exposure do not result in contrasting fault pattern to both sides of the Gejiu Fault (Fig. 1c) and the distribution of major mineralization in the eastern sector (Jiang et al., 1997) is controlled by faults (Fig. 10). Therefore, post-mineralization tectonic processes do not account for the obvious differences in fault pattern between the two sectors.

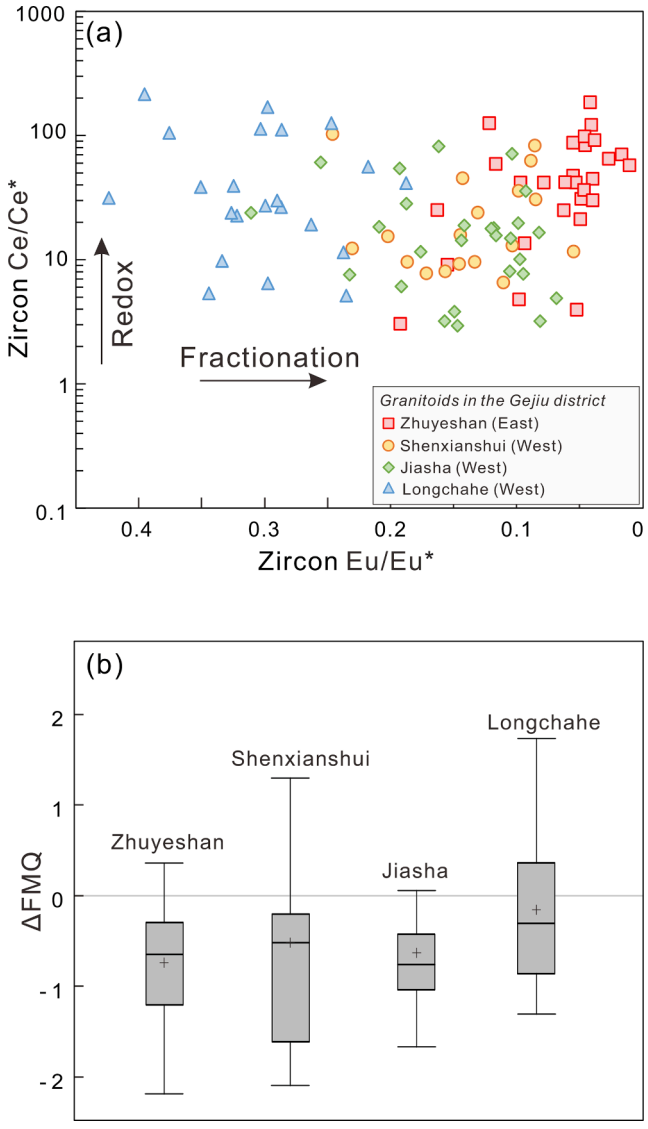

Fig. 6. (a) Zircon Eu/Eu* vs. Ce/Ce* diagram for granitoids from the Gejiu area. Similar Ce/Ce* values for the various intrusions suggest that granitoids to the east and west of the Gejiu Fault had similar oxygen fugacity, whereas the relatively large variation in Eu/Eu* values reflects the variable extent of fractionation among the various granitoids and among samples of individual intrusions. (b) Box diagram showing the ΔFMQ values of the Zhuyeshan, Shenxianshui, Jiasha, and Longchahe granitoids. The ΔFMQ values are close or below the FMQ, demonstrating that the various granitoids have similar oxygen fugacity and are reduced.

The granite emplacement occurred during late Cretaceous strike-slip movement along the conjugate Gejiu-Ailaoshan fault system and the local orientation of the stress field may have had a dominant role on the distribution of mineralization, in particular whether economic deposits could evolve at all. In the following sections, we demonstrate how Cretaceous strike-slip movement along the conjugate Gejiu-Ailaoshan fracture system can control the distribution of Sn mineralization in the Gejiu district, in particular the selective occurrence of major deposits in the eastern sector. Note, this explanation does not rule out the possibility that there have been (now eroded) Sn deposits in the western sector, but it makes the possibility of major Sn deposits in the western sector rather unlikely.

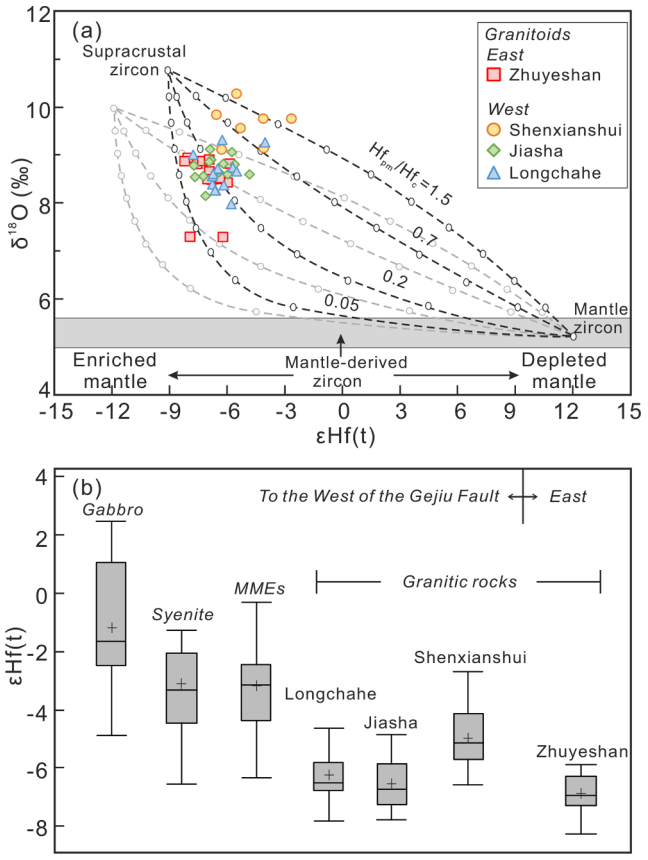

Fig. 7. (a) Plot of zircon εHf(t) vs. $\delta^{18}O$ for granitoids to both sides of the Gejiu Fault (modified after Li et al., 2009). Binary mixing curves are shown for typical crustal and mantle end members. The curves are calculated for different Hf concentration ratios of the two end members (c = crust, pm = primitive mantle). Tick marks are set at 10% intervals. Note, the composition of the actual crustal end member involved in the formation of the Cretaceous granites in the Gejiu area is not well known, as its εHf depends on the average crustal residence time of the material contributing to the crustal source and $\delta^{18}O$ depends on the weathering history of the crustal end member. We used Proterozoic metasedimentary rocks from South China as crustal end member (Zhang et al., 2006). For comparison, Li et al. (2009) used the ~ 230 Ma Darongshan cordierite granites as crustal end member (light grey dotted lines). The Zhuyeshan, Jiasha, and Longchahe granitoids fall in a narrow and overlapping cluster and show some incorporation of mantle derived magma. Data from the Shenxianshui granite in part have higher $\delta^{18}O$ values. The Cretaceous granitoids of the Gejiu area are dominantly derived from metasedimentary rocks. (b) Box diagram comparing the εHf(t) values of the Zhuyeshan granite to the east of the Gejiu Fault with the εHf(t) values of granitoids, mafic microgrannular enclaves, syenites, and gabbros to the west of the Gejiu Fault. Data for the mafic microgranular enclaves, syenites, and gabbros are from Cheng et al. (2013b).

5.3. *Evidence for tectonic controlled tin mineralization*

There is growing evidence that the tectonic setting during the emplacement of tin granites controls the concentration of Sn by magmatic fluids. For instance, the voluminous Tertiary leucogranites of the Greater Himalayas and the Cornubian batholiths of SW England have similar geochemical pattern (see Fig. 15 in Romer and Kroner, 2016), but contrasting extent of Sn mineralization. The Cornubian batholiths host the most important Sn province in Europe. These early Permian granites (Chen et al., 1993) were emplaced in an extensional setting, subsequent to the Variscan orogeny when the entire Variscan belt was under extension as mirrored in the distribution of Permian volcanism and Permian fault-bound sedimentary basins (Neumann et al., 2004; Ziegler and Dèzes, 2006). In contrast, there is no economically relevant Sn mineralization known to be associated with the

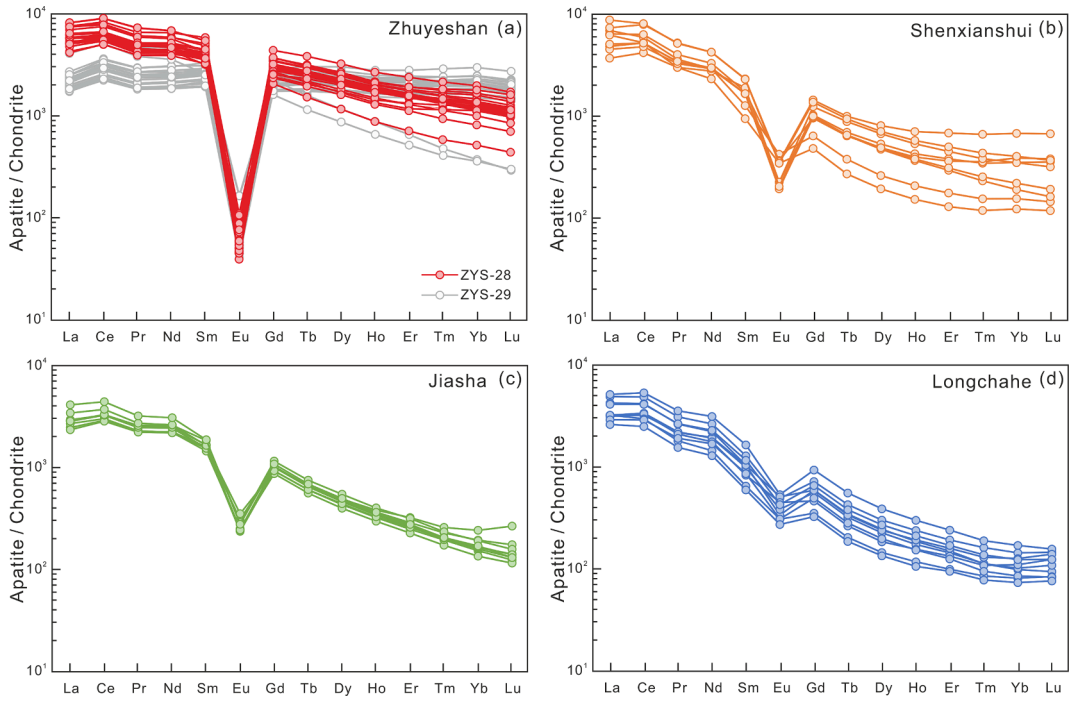

Fig. 8. Rare earth element pattern of apatite from the (a) Zhuyeshan, (b) Shenxianshui, (c) Jiasha, and (d) Longchahe granitoids normalized to Chondrite (Sun and McDonough, 1989). The patterns generally are characterized by LREE-enrichment and HREE-depletion with variably negative Eu anomalies. Apatite from the whole rock sample ZYS-29 show a relatively flat REE pattern.

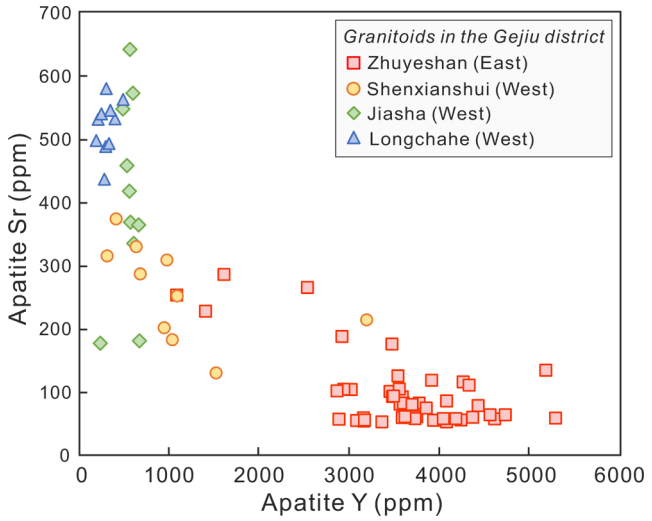

Fig. 9. Plot of apatite Sr (ppm) vs. Y (ppm) for granitoids to the east and west sides of the Gejiu Fault. The Zhuyeshan and Shenxianshui granites, which have the geochemical fingerprints of fertile Sn-granites, have high Y contents and show a negative correlation between Y and Sr contents, whereas the Jiasha and Longchahe granitoids are characterized by relatively low Y contents and variable Sr contents.

syncollisional Himalayan leucogranites to the north of the main Himalayan thrust, even though cassiterite is known to occur in some of these granites (typically found as byproduct in heavy mineral concentrates prepared for zircon dating; pers. comm. John Cottle, UCSB). The Himalayan Tertiary granites were emplaced in a compressional setting during the ongoing Cenozoic India Asia collision (Crawford and Windley, 1990).

In the Central European Variscides, the entire Erzgebirge – Fichtelgebirge Zone, another major Variscan Sn province, hosts late Variscan tin granites. Because the same heat source is affecting the same protoliths within the Erzgebirge – Fichtelgebirge Zone (for details see Romer and Kroner, 2015), the tin granites within this zone belong to the same geochemical suite (Siebel et al., 1997; Förster, 1999; Förster and Romer, 2010). The striking difference in the distribution of Sn mineralization between the Erzgebirge and Fichtelgebirge areas is related to the contrasting tectonic setting during late Variscan granite emplacement. At the time of granite emplacement, the Erzgebirge constitutes a late orogenic transtensional domain (e.g., Willner et al., 2000), whereas the adjacent Fichtelgebirge Zone is characterized by late Variscan compression (Franke and Stein, 2000). Both domains are separated by a huge fault zone, along which a major granite suite was emplaced. The tin granites of the Erzgebirge host important tin mineralization, whereas those in the Fichtelgebirge only show minor mineralization without economic importance.

The contrasting development of mineralization in Cornwall and the Greater Himalayas – as well as in the Erzgebirge-Fichtelgebirge Zone of the Central European Variscides – indicates that apart from the geochemical character of the granites, the tectonic regime during magma emplacement may be important for the development of mineralization. It seems, that compressional / transpessional settings do not allow for the formation of large-scale tin deposits, whereas extensional / transtensional settings are favorable for the formation of tin deposits. This is analogue to the formation of hydrothermal vein-type deposits (Sibson, 1996). Extensional / transtensional tectonics leads to the formation of steeply-dipping open fluid pathways allowing for the vertical ascent of mineralizing fluids. In contrast, compressional regimes do not result in the formation of such open and interconnected fluid networks. We apply the principles of macro-scale fracturing during the formation of hydrothermal vein-type deposits (Sibson, 1996) and argue that the interplay of ascending fluids and interconnected microcracks is essential for the late-stage redistribution of Sn and the formation of primary granite-related Sn deposits.

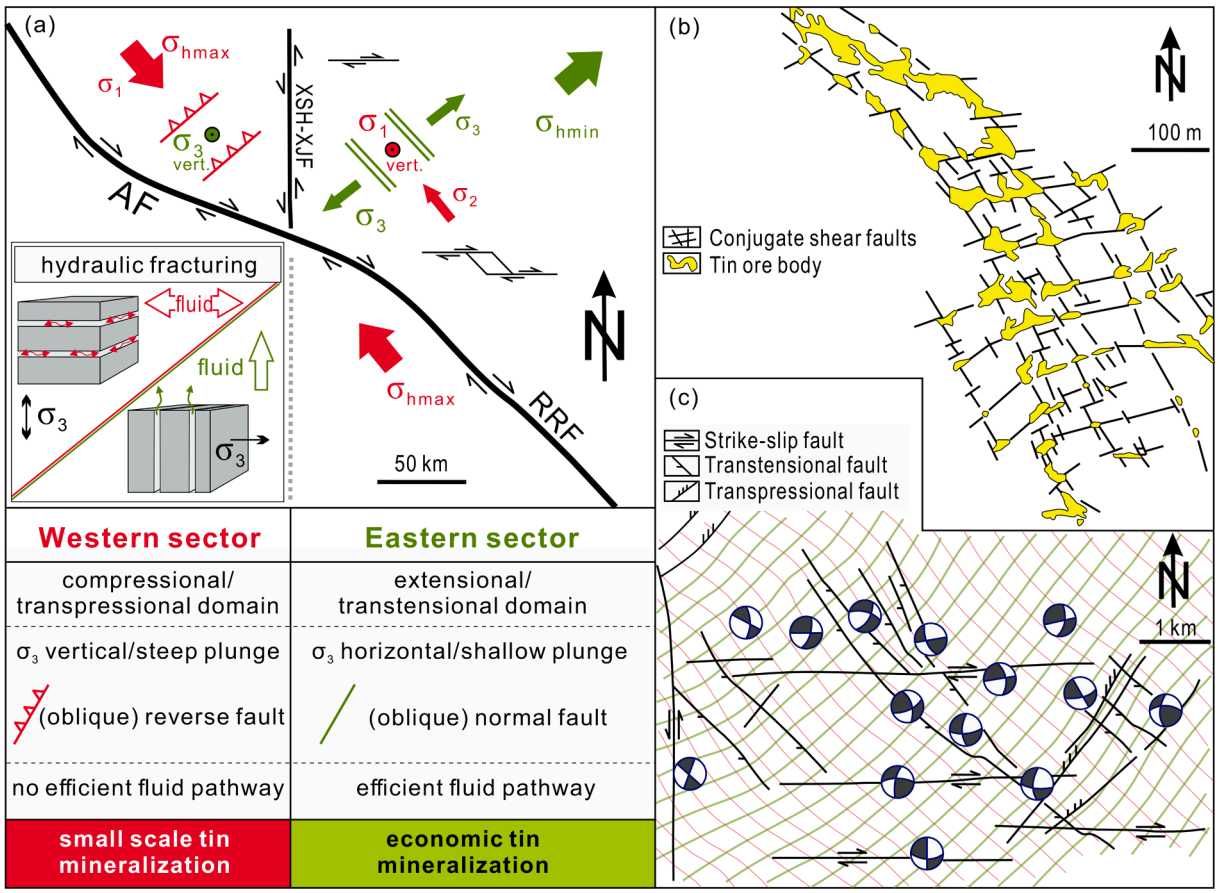

Fig. 10. (a) Conceptual model to explain the contrasting distribution of granite-related mineralization in the areas to the east and west of the Gejiu Fault (XSH-XJF). In the late Cretaceous sinistral strike slip Gejiu Fault constitutes the conjugate shear fracture to the dextral Ailaoshan Fault (AF) – Red River Fault (RRF) zone. This conjugate system is responsible for differences of the regional stress field. In the west, a vertically oriented sigma 3 resulted in horizontal tension gashes (microcracks) due to hydraulic fracturing during late-stage magmatic fluid escape. Such a fracture network hampered the vertical ascent of fluids and the mobilization and redistribution of Sn. Instead, cassiterite crystallized disperse distributed in the granite. In the eastern sector, sigma 3 is horizontally oriented allowing for vertical fluid escape. This strikingly contrasting distribution of fractures and faults provided efficient fluid pathways that eventually allowed for extensive mineralization in the upper parts of the granite and the country rocks in the roof. Mineralization occurred in transtensional shear zones along dilatational jogs along E-W oriented dextral strike slip fault (Jiang et al., 1997). (b) Relation between conjugate fault zones and mineralization at the Malage Sn deposit (Gejiu district). Figure is from Jiang et al. (1997). (c) Relation between fault pattern and stress distribution in the surroundings of the Malage Sn deposits (Gejiu district). Conjugate shear joints (upper hemisphere projection) showing sectors of maximum (dark fields) and minimum (light field) stress. The trajectories of maximum (red) and minimum (green) stress represent interpretations of the joint pattern. Figure simplified from Jiang et al. (1997).

5.4. *The role of fluids and the need of an efficient fluid pathway*

During late-stage crystallization, the granitic melt becomes saturated in fluids that eventually exsolve. Generally, it is assumed that most metals partition into the fluid (e.g., Heinrich, 1990) and eventually form mineralization within the granite or in the wall rocks. Recent experimental work showed that some ore elements do not partition preferentially into the exsolving magmatic fluid. For instance, W partitions preferentially into the fluid, but Sn partitions preferentially into the melt (Schmidt, 2018; Schmidt et al., 2020). At the scale of an individual intrusion, this contrasting partitioning behavior may account for the spatial separation of Sn and W. At the scale of entire mineral districts, however, other factors, such as melting temperature of sedimentary protoliths, control the distribution of W and Sn mineralization (Yuan et al., 2019).

Preferential partitioning of Sn into the granitic melt during late stage fluid exsolution eventually leads to granites with disperse cassiterite crystals or with Sn being substituted into silicate minerals, such as titanite and biotite (Breiter and Scharbert, 1995; Wang et al., 2013). Later fluids percolating through these rocks may dissolve magmatic cassiterite and alter Sn-hosting silicates. These later fluids may be magmatic fluids from other, later crystallizing parts of the intrusion (Schmidt et al., 2020) or external fluids that become heated by the intrusion (e.g., Xu et al., 2021). Tin mobilization by Cl-rich fluids is particularly efficient at temperatures above 400 °C (Schmidt, 2018). If these fluids also have a low pH, they may induce the formation of greisens and the precipitation of Sn as cassiterite (Schmidt et al., 2020).

The final stages of metal concentration involves redistribution of metals via fluids and requires efficient fluid pathways both for mobilization and for concentrating the metals to a deposition volume. Such a network of intersecting pathways must be present at least in the apical part of the granite, where the last-crystallizing melt concentrated before fluid exsolution, and transport of metals that partition into the buoyant fluids to higher crustal levels. Hydraulic (micro) fracturing due to fluid overpressure is able to produce fluid pathways even at higher temperatures (e.g., Lefebvre et al., 2019, Fig. 3). Fluid overpressure reduces the effective stress and may result in tensional fractures (e.g., Twiss and Moores, 1992). The orientation of such fractures is orthogonal to the least principal stress axis, i.e, orthogonal to **sigma 3**. An anastomosing network of preferentially vertically oriented tensile fractures requires a horizontal **sigma 3**. Such an orientation of the stress tensor is realized in extensional and strike-slip settings and their combination, i.e., in transtensional settings. In contrast, hydraulic fracturing in compressional regimes should result in the preferred formation of horizontal

tensile fractures caused by the vertically arranged **sigma 3**. Such a preferred orientation hampered the vertical ascent of the exsolved fluid and dissolved metals do not concentrate in veins, greisen, or skarn type mineralization. Instead, ore minerals are disperse distributed within the apical parts of the granite. The contrasting orientations of **sigma 3** explain the striking difference between tin granites of Cornwall and the Greater Himalayas. Moreover, if there is a regional contrast in deformation, the adjacent compressional and extensional domains are separated by fault zones, which explains the presence and absence of economically important tin deposits in the Erzgebirge – Fichtelgebirge area, respectively, and – by analogy – the eastern and western sectors of the Gejiu area.

5.5. *Tectonic model for the spatial distribution of the tin deposits in the Gejiu district*

We propose that the Gejiu-Ailaoshan fault-system controls the spatial distribution of large Sn deposits in the Gejiu district. The Ailaoshan Fault and the conjugate Gejiu Fault, which is separating the eastern and western sectors, intersect at an angle of ca. 70° and 110°, respectively (Fig. 10). Dextral strike-slip at the Ailaoshan Fault coeval to sinistral strike-slip at the Gejiu Fault results in conjugate Mohr-Coulomb faults, i.e., shear fractures. The western sector is characterized by an acute angle between **sigma 1** and both strike-slip faults. Strain partitioning leads to compressional / transpressional deformation in the western sector, whereas the eastern sector experiences predominantly extensional / transtensional deformation. In such a scenario the NW-SE striking fractures act as (oblique) normal faults, whereas the dominant NE-SW striking faults represent reverse faults (Fig. 10).

Syntectonic granites to the west of the Gejiu Fault intruded and crystalized in a compressive setting and those to the east intruded in a dilatative setting. In contrast to the western sector, the orientation of the principal stress axis, i.e., **sigma 3** in the eastern sector was nearly horizontal, allowing for the formation of an efficient fluid pathway during the final hydrothermal stage. The interconnected and predominantly vertical oriented micro-fractures in the granite resulted in predominantly vertical escape of the Sn bearing fluids culminating in voluminous mineralization of the granite and the country rocks of the roof zone. In contrast, the western sector is characterized by a steeply dipping **sigma 3**. Due to fluid overpressure microcracking in the granites resulted in predominantly sub-horizontal tension gashes. This structural pattern does not allow for important vertical fluid migration into the roof of the granites and their host rocks. Cassiterite that had crystallized disperse distributed within the granite may become dissolved locally by later fluids, but Sn did not concentrate into major deposits.

The Ailaoshan and the Gejiu faults had been repeatedly reactivated as sinistral and dextral faults (e.g., Morley, 2012; Chen et al., 2019). Thus, the same faults that controlled the contrasting mineralizations in a transpressional unmineralized horst in the west and a less uplifted transtensional mineralized domain in the east, also control later tectonic processes, in particular the differential uplift of the two blocks. The granites in the western area intruded into the siliciclastic rocks of the Falang Formation and the eroded units above, whereas in the eastern area the granites only intruded into the Gejiu Formation and did not reach the stratigraphically overlying rocks of the Falang Formation. Thus, the present erosion level is unrelated with the emplacement level of the granites.

6. Conclusions

The granitic rocks to the east (Zhuyeshan) and west (Shenxianshui, Jiasha, and Longchahe) of the Gejiu Fault show similarities in terms of emplacement ages, source rocks, melting temperature, oxygen fugacity, and extent of fractionation, based on (i) zircon U-Pb ages around 83 Ma; (ii) low whole rock εNd(t) and zircon εHf(t) values (−9.0 to − 7.0 and − 8.2 to − 2.7, respectively), and high zircon $\delta^{18}O$ values (7.30 to 10.28 ‰), as well as Mesoproterozoic Nd and Hf two-stage model ages; (iii) high zircon saturation temperatures (760 to 831 ℃); and (iv) calculated $logfO_2$ values falling below FMQ buffer. Furthermore, the Zhuyeshan and Shenxianshui granites have flat UCC-normalized REE patterns with deep Eu anomalies and tetrade effects, and marked enrichments of Li, Rb, Cs, Ta, Hf, and U and depletions of Sr, Ba, and Zr. The geochemical fingerprints of these granitic rocks demonstrate that the absence of major deposits to the west of the Gejiu Fault is not due to the absence of fertile granitic rocks. The contrasting distribution of major deposits does not reflect different levels of exposure (with potential deposits to the west of the fault having been eroded). Instead, the sectors to the east and west of the Gejiu Fault, which have different fault pattern experienced contrasting tectonic settings during the emplacement of the Cretaceous granites. Dextral strike-slip along the Ailaoshan Fault and sinistral strike-slip along the Gejiu Fault result in an extensional / transtensional setting in the eastern sector, which favors the circulation of late-magmatic fluids in the roof zones of the granites leading to the formation of major Sn mineralization, and a compressional and transpressional setting in the western sector, which does not favor large-scale fluid circulation and did not lead to significant mineralization.

Declaration of Competing Interest

The authors declare that they have no known competing financial interests or personal relationships that could have appeared to influence the work reported in this paper.

Acknowledgments

We are grateful to K.K. Sun, X.L. Cui, H.Y. Cheng, and J.P. Li for help during sampling and to C. Yu, Z.Y. Chen, X.D. Chen, and F.Y. Wang for help with sample preparation and analytical work. We thank two anonymous reviewers and Editor Chen Huayong for helpful comments. This research was financially supported by the National Natural Science Foundation of China (grant number 91855217) and National Basic Research Program of China (grant number 2015CB452606). The work of Rong Xu at GFZ was supported by a CSC student scholarship (201906400057).

Appendix A. Supplementary data

Supplementary data to this article can be found online at https://doi.org/10.1016/j.oregeorev.2022.105004.

References

308 Geological Party, 1984. Geology of tin deposit in Gejiu area. Metallurgical Industry Publishing House, Beijing, pp. 256 (in Chinese).

Azadbakht, Z., Lentz, D.R., McFarlane, C.R.M., Whalen, J.B., 2020. Using magmatic biotite chemistry to differentiate barren and mineralized Silurian-Devonian granitoids of New Brunswick. Canada. Contributions to Mineralogy and Petrology 175. https://doi.org/10.1007/s00410-020-01703-2.

Ballard, J.R., Michael Palin, J., Campbell, I.H., 2002. Relative oxidation states of magmas inferred from Ce(IV)/Ce(III) in zircon: application to porphyry copper deposits of northern Chile. Contrib. Miner. Petrol. 144, 347–364.

Ballouard, C., Poujol, M., Boulvais, P., Branquet, Y., Tartèse, R., Vigneresse, J.-L., 2016. Nb-Ta fractionation in peraluminous granites: A marker of the magmatic-hydrothermal transition. Geology 44, 231–234.

Barbero, L., 1995. Granulite-facies metamorphism in the Anatectic Complex of Toledo, Spain: Late Hercynian tectonic evolution by crustal extension. Journal of the Geological Society 152, 365–382.

Belousova, E.A., Griffin, W.L., O'Reilly, S.Y., Fisher, N.I., 2002. Apatite as an indicator mineral for mineral exploration: trace-element compositions and their relationship to host rock type. J. Geochem. Explor. 76, 45–69.

Breiter, K., Müller, A., Leichmann, J., Gabašová, A., 2005. Textural and chemical evolution of a fractionated granitic system: the Podlesí stock, Czech Republic. Lithos 80, 323–345.

Breiter, K., Scharbert, S., 1995. The Homolka magmatic centre—An example of late Variscan ore bearing magmatism in the Southbohemian batholith (southern Bohemia, Northern Austria). Jb. Geol. Bundesanst. 138, 9–25.

Burnham, A.D., Berry, A.J., 2012. An experimental study of trace element partitioning between zircon and melt as a function of oxygen fugacity. Geochim. Cosmochim. Acta 95, 196–212.
Cao, M.J., Zhou, Q.F., Qin, K.Z., Tang, D.M., Evans, N.J., 2013. The tetrad effect and geochemistry of apatite from the Altay Koktokay No. 3 pegmatite, Xinjiang, China: implications for pegmatite petrogenesis. Mineral. Petrol. 107, 985–1005.
Chen, J., Halls, C., Stanley, C.J., 1992a. Tin-bearing skarns of South China: Geological setting and mineralogy. Ore Geol. Rev. 7, 225–248.
Chen, J., Halls, C., Stanley, C.J., 1992b. Mineral association and mineralogical criteria for the formation condition of a B-F-Sn-Bi skarn in Damoshan, Gejiu tin field. Southwest China. Chin. Journal of Geochemistry 11, 140–155.
Chen, X., Burg, J.P., Liu, J., Qi, Y., Fan, W., Wang, K., 2019. Multistage remobilization of the southwestern margin of the South China Plate: Insights from zircon U-Pb geochronology and Hf isotope of granitic rocks from the Yao Shan Complex, Southeastern Tibet Plateau. Tectonics 38, 621–640.
Chen, Y., Clark, A.H., Farrar, E., Wasteneys, H.A.H.P., Hodgson, M.J., Bromley, A.V., 1993. Diachronous and independent histories of plutonism and mineralization in the Cornubian Batholith, southwest England. Journal of the Geological Society 150, 1183–1191.
Cheng, Y.B., Spandler, C., Kemp, A., Mao, J.W., Rusk, B.G., Hu, Y., Blake, K., 2019. Controls on cassiterite (SnO_2) crystallization: Evidence from cathodoluminescence, trace-element chemistry, and geochronology at the Gejiu Tin District. Am. Mineral. 104, 118–129.
Cheng, Y.B., Spandler, C., Mao, J.W., Rusk, B., 2012a. Granite, gabbro and mafic microgranular enclaves in the Gejiu area, Yunnan Province, China: a case of two-stage mixing of crust- and mantle-derived magmas. Contrib Mineral Petrol 164, 659–676.
Cheng, Y.B., Mao, J.W., Yang, Z.X., 2012b. Geology and vein tin mineralization in the Dadoushan deposit, Gejiu district, SW China. Miner Deposita 47, 701–712.
Cheng, Y.B., Mao, J.W., Chang, Z.S., Pirajno, F., 2013a. The origin of the world class tin-polymetallic deposits in the Gejiu district, SW China: Constraints from metal zoning characteristics and ^{40}Ar–^{39}Ar geochronology. Ore Geol. Rev. 53, 50–62.
Cheng, Y.B., Mao, J.W., Spandler, C., 2013b. Petrogenesis and geodynamic implications of the Gejiu igneous complex in the western Cathaysia block, South China. Lithos 175–176, 213–229.
Cheng, Y.B., Mao, J.W., 2010. Age and geochemistry of granites in Gejiu area, Yunnan province, SW China: constraints on their petrogenesis and corresponding tectonic setting. Lithos 120, 258–276.
Chu, M.F., Wang, K.L., Griffin, W.L., Chung, S.L., O'Reilly, S.Y., Pearson, N.J., Iizuka, Y., 2009. Apatite composition: Tracing petrogenetic processes in Transhimalayan granitoids. J. Petrol. 50, 1829–1855.
Crawford, M.B., Windley, B.F., 1990. Leucogranites of the Himalaya/Karakoram: implications for magmatic evolution within collisional belts and the study of collision-related leucogranite petrogenesis. J. Volcanol. Geoth. Res. 44, 1–19.
Deng, J., Qiu, K.F., Wang, Q.F., Goldfarb, R.J., Yang, L.Q., Zi, J.W., Geng, J.Z., Ma, Y., 2020a. In-situ dating of hydrothermal monazite and implications on the geodynamic controls of ore formation in the Jiaodong gold province, Eastern China. Econ. Geol. 115, 671–685.
Deng, J., Wang, Q.F., Li, G.J., Santosh, M., 2014. Cenozoic tectono-magmatic and metallogenic processes in the Sanjiang region, southwestern China. Earth Sci. Rev. 138, 268–299.
Deng, J., Yang, L.Q., Groves, D.I., Zhang, L., Qiu, K.F., Wang, Q.F., 2020b. An integrated mineral system model for the gold deposits of the giant Jiaodong province, eastern China. Earth-Science Reviews 208, 103274.
Ferry, J.M., Watson, E.B., 2007. New thermodynamic models and revised calibrations for the Ti-in-zircon and Zr-in-rutile thermometers. Contrib. Miner. Petrol. 154, 429–437.
Fogliata, A.S., Báez, M.A., Hagemann, S.G., Santos, J.O., Sardi, F., 2012. Post-orogenic, Carboniferous granite-hosted Sn–W mineralization in the Sierras Pampeanas Orogen, Northwestern Argentina. Ore Geol. Rev. 45, 16–32.
Förster, H.-J., 1999. The chemical composition of uraninite in Variscan granites of the Erzgebirge. Germany, Mineralogical Magazine 63, 239–252.
Förster, H.-J., Romer, R.L., 2010. Carboniferous magmatism. In: Linnemann, U., Romer, R. L. (Eds.), Pre-Mesozoic Geology of Saxo-Thuringia: From the Cadomian Active Margin to the Variscan Orogen, Schweizerbart, 287–308.
Franke, W., Stein, E., 2000. Exhumation of high-grade rocks in the Saxo-Thuringian Belt: geological constraints and geodynamic concepts. Geological Society, London, Special Publications 179, 337–354.
Gardiner, N.J., Searle, M.P., Robb, L.J., Morley, C.K., 2015. Neo-Tethyan magmatism and metallogeny in Myanmar – An Andean analogue? J. Asian Earth Sci. 106, 197–215.
Gardiner, N.J., Robb, L.R., Morley, C.K., Searle, M.P., Cawood, P.A., Whitehouse, M.J., Kirkland, C.L., Roberts, N.M.W., Myint, T.A., 2016. The tectonic and metallogenic framework of Myanmar: A Tethyan mineral system. Ore Geol. Rev. 79, 26–45.
Gardiner, N.J., Hawkesworth, C.J., Robb, L.J., Whitehouse, M.J., Roberts, N.M.W., Kirkland, C.L., Evans, N.J., 2017. Contrasting Granite Metallogeny through the Zircon Record: A Case Study from Myanmar. Sci. Rep. 7, 748.
Guo, J., 2019. Tin mineralization events and fertility of granitoids in the Youjiang Basin, South China: The Gejiu and Dachang Sn-polymetallic districts as examples. Doctoral thesis, University of Chinese Academy of Sciences (in Chinese with English abstract).
Guo, J., Zhang, R.Q., Li, C.Y., Sun, W.D., Hu, Y.B., Kang, D.M., Wu, J.D., 2018. Genesis of the Gaosong Sn-Cu deposit, Gejiu district, SW China: Constraints from in situ LA-ICP-MS cassiterite U-Pb dating and trace element fingerprinting. Ore Geol. Rev. 92, 627–642.
He, F.P., Wang, Z.H., Zu, Y.C., Wang, L., Wang, J., 2014. Identifying and Assessment of Mineralization Information Associated with Sn-polymetallic Mineralization in the Western Gejiu District, Yunnan. Acta Scientiarum Naturalium Universitatis Sunyatseni 53, 115–120 in Chinese with English abstract.
Heinrich, C.A., 1990. The chemistry of hydrothermal tin (−tungsten) ore deposition. Econ. Geol. 85, 457–481.
Hu, L., Cawood, P.A., Du, Y., Yang, J., Jiao, L., 2015. Late Paleozoic to Early Mesozoic provenance record of Paleo-Pacific subduction beneath south China. Tectonics 34, 986–1008.
Hu, P.C., Zhu, W.G., Zhong, H., Zhang, R.Q., Zhao, X.Y., Mao, W., 2021. Late Cretaceous granitic magmatism and Sn mineralization in the giant Yinyan porphyry tin deposit, South China: constraints from zircon and cassiterite U-Pb and molybdenite Re–Os geochronology. Miner. Deposita 56, 743–765.
Ishihara, S., Sawata, H., Arpornsuwan, S., Busaracome, P., Bungbrakearti, N., 1979. The magnetite-series and ilmenite-series granitoids and their bearing on tin mineralization, particularly of the Malay Peninsula region. Geological Society of Malaysia, Bulletin. 11, 103–110.
Jiang, Z.W., Oliver, N.H.S., Barr, T.D., Power, W.L., Ord, A., 1997. Numerical modeling of fault-controlled fluid flow in the genesis of tin deposits of the Malage Ore Field, Gejiu Mining District, China. Econ. Geol. 92, 228–247.
Lefebvre, M.G., Romer, R.L., Glodny, J., Kroner, U., Roscher, M., 2019. The Hämmerlein skarn-hosted polymetallic deposit and the Eibenstock granite associated greisen, western Erzgebirge, Germany: two phases of mineralization—two Sn sources. Miner. Deposita 54, 193–216.
Lehmann, B., 1990. Metallogeny of Tin. Springer-Verlag, Berlin.
Lehmann, B., Ishihara, S., Michel, H., Miller, J., Rapela, C.W., Sanchez, A., Tistl, M., Winkelmann, L., 1990. The Bolivian tin province and regional tin distribution in the Central Andes; a reassessment. Econ. Geol. 85, 1044–1058.
Li, X.H., Li, W.X., Wang, X.C., Li, Q.L., Liu, Y., Tang, G.Q., 2009. Role of mantle-derived magma in genesis of early Yanshanian granites in the Nanling Range, South China: in situ zircon Hf-O isotopic constraints. Sci. China, Ser. D Earth Sci. 52, 1262–1278.
Liew, T.C., Hofmann, A.W., 1988. Precambrian crustal components, plutonic associations, plate environment of the Hercynian Fold Belt of central Europe: Indications from a Nd and Sr isotopic study. Contrib. Miner. Petrol. 98, 129–138.
Liu, Y., Hu, Z., Gao, S., Günther, D., Xu, J., Gao, C., Chen, H., 2008. In situ analysis of major and trace elements of anhydrous minerals by LA-ICP-MS without applying an internal standard. Chem. Geol. 257, 34–43.
Loucks, R.R., Fiorentini, M.L., Henríquez, G.J., 2020. New magmatic oxybarometer using trace elements in zircon. J. Petrol. 61, egaa034.
Lu, H.J., Liu, J.S., 2020. The geologic structure and prospecting potentiality of Gejiu Sn deposit W area, Yunnan. Yunnan Geology 39, 166–173 in Chinese with English abstract.
Lu, Y.J., Loucks, R.R., Fiorentini, M., Campbell McCuaig, T., Evans, N.J., Yang, Z.M., Hou, Z.Q., Kirkland, C.L., Parra-Avila, L.A., Kobussen, A., 2016. Zircon Compositions as a Pathfinder for Porphyry Cu ± Mo ± Au Deposits. Society of Economic Geologists, Special Publication 19, 329–347.
Ludwig, K.R., 2003. User's Manual for Isoplot 3.0: a geochronological Toolkit for Microsoft Excel. Berkeley Geochronology Center Special. Publication 4, 71.
Mao, J.W., Cheng, Y.B., Chen, M.H., 2013. Major types and time–space distribution of Mesozoic ore deposits in South China and their geodynamic settings. Miner Deposita 48, 267–294.
Mao, J., Ouyang, H., Song, S., Santosh, M., Yuan, S., Zhou, Z., Zheng, W., Liu, H., Liu, P., Cheng, Y., Chen, M., 2019. Geology and metallogeny of tungsten and tin deposits in China. Society of Economic Geologists, Special Publication 22, 411–482.
Metcalfe, I., 2002. Permian tectonic framework and palaeogeography of SE Asia. J. Asian Earth Sci. 20, 551–566.
Miller, C.F., McDowell, S.M., Mapes, R.W., 2003. Hot and cold granites? Implications of zircon saturation temperatures and preservation of inheritance. Geology 31, 529–532.
Morley, C.K., 2012. Late Cretaceous-early Palaeogene tectonic development of SE Asia. Earth-Sci. Rev. 115, 37–75.
Myint, A.Z., Li, H., Mitchell, A., Selby, D., Wagner, T., 2021. Geology, mineralogy, ore paragenesis, and molybdenite Re-Os geochronology of Sn-W (-Mo) mineralization in Padatgyaung and Dawei, Myanmar: Implications for timing of mineralization and tectonic setting. J. Asian Earth Sci. 212, 104725.
Neumann, E.R., Wilson, M., Heeremans, M., Spencer, E.A., Obst, K., Timmerman, M.J., Kirstein, L., 2004. Carboniferous-Permian rifting and magmatism in southern Scandinavia, the North Sea and northern Germany: a review. Geological Society, London, Special Publications 223, 11–40.
Olade, M.A., 1980. Geochemical characteristics of tin-bearing and tin-barren granites, northern Nigeria. Econ. Geol. 75, 71–82.
Palma, G., Barra, F., Reich, M., Valencia, V., Simon, A.C., Vervoort, J., Leisen, M., Romero, R., 2019. Halogens, trace element concentrations, and Sr-Nd isotopes in apatite from iron oxide-apatite (IOA) deposits in the Chilean iron belt: Evidence for magmatic and hydrothermal stages of mineralization. Geochim. Cosmochim. Acta 246, 515–540.
Paton, C., Woodhead, J.D., Hellstrom, J.C., Hergt, J.M., Greig, A., Maas, R., 2010. Improved laser ablation U-Pb zircon geochronology through robust downhole fractionation correction. Geochem. Geophys. Geosyst. 11, 1–36.
Romer, R.L., Kroner, U., 2015. Sediment and weathering control on the distribution of Paleozoic magmatic tin–tungsten mineralization. Miner. Deposita 50, 327–338.
Romer, R.L., Kroner, U., 2016. Phanerozoic tin and tungsten mineralization—Tectonic controls on the distribution of enriched protoliths and heat sources for crustal melting. Gondwana Res. 31, 60–95.
Rudnick, R.L., Gao, S., 2003. Composition of the continental crust. The Crust. Elsevier 1–64.
Sato, K., 2012. Sedimentary crust and metallogeny of granitoid affinity: Implications from the geotectonic histories of the Circum-Japan Sea Region, Central Andes and Southeastern Australia. Resour. Geol. 62, 329–351.

Schmidt, C., 2018. Formation of hydrothermal tin deposits: Raman spectroscopic evidence for an important role of aqueous Sn(IV) species. Geochim. Cosmochim. Acta 220, 499–511.
Schmidt, C., Romer, R.L., Wohlgemuth-Ueberwasser, C.C., Appelt, O., 2020. Partitioning of Sn and W between granitic melt and aqueous fluid. Ore Geol. Rev. 117, 103263.
Searle, M.P., Robb, L.J., Gardiner, N.J., 2016. Tectonic processes and metallogeny along the Tethyan Mountain Ranges of the Middle East and South Asia (Oman, Himalaya, Karakoram, Tibet, Myanmar, Thailand, Malaysia). Society of Economic Geologists, Special Publication 19, 301–327.
Sibson, R.H., 1996. Structural permeability of fluid-driven fault-fracture meshes. Journal of Structural Geology 18, 1301–1042.
Siebel, W., Raschka, H., Irber, W., Kreuzer, H., Lenz, K.L., Höhndorf, A., Wendt, I., 1997. Early Palaeozoic acid magmatism in the Saxothuringian Belt: new insights from a geochemical and isotopic study of orthogneisses and metavolcanic rocks from the Fichtelgebirge, SE Germany. J. Petrol. 38, 203–230.
Sloan, R.A., Elliott, J.R., Searle, M.P., Morley, C.K., 2017. Active tectonics of Myanmar and the Andaman Sea. Geological Society, London, Memoirs 48, 19–52.
Stussi, J.-M., 1989. Granitoid chemistry and associated mineralization in the French Variscan. Econ. Geol. 84, 1363–1381.
Sun, S.S., McDonough, W.F., 1989. Chemical and isotopic systematics of oceanic basalts: implications for mantle composition and processes. In: Saunders, A.D., & Norry, M. J., (eds) Magmatism in the Ocean Basins. Geological Society, London, Special Publications 42, 313–346.
Tan, S.C., Hu, X.G., Jin, Y.Z., Chen, J., Chen, F., 2013. Extraction of metallogenic information and prospecting prediction based on Landsat TM in Gejiu tin deposit area. Metal Mine 442 (4), 101–105 in Chinese with English abstract.
Twiss, R.J., Moores, E.M., 1992. Structural Geology. Freeman, New York, W.H.
Viruete, J.E., Indares, A., Arenas, R., 2000. P-T paths derived from garnet growth zoning in an extensional setting: An example from the Tormes gneiss dome (Iberian massif, Spain). J. Petrol. 41, 1489–1515.
Wai-Pan Ng, S., Whitehouse, M.J., Searle, M.P., Robb, L.J., Ghani, A.A., Chung, S.-L., Oliver, G.J.H., Sone, M., Gardiner, N.J., Roselee, M.H., 2015. Petrogenesis of Malaysian granitoids in the Southeast Asian tin belt: Part 2. U-Pb zircon geochronology and tectonic model. Geol. Soc. Am. Bull. 127, 1238–1258.
Wang, C.M., Deng, J., Carranza, E.J.M., Santosh, M., 2014. Tin metallogenesis associated with granitoids in the southwestern Sanjiang Tethyan Domain: Nature, deposit types, and tectonic setting. Gondwana Res. 26, 576–593.
Wang, R.C., Xie, L., Chen, J., Yu, A.P., Wang, L.B., Lu, J.J., Zhu, J.C., 2013. Tin-carrier minerals in metaluminous granites of the western Nanling Range (southern China): Constraints on processes of tin mineralization in oxidized granites. J. Asian Earth Sci. 74, 361–372.
Watson, E.B., Harrison, T.M., 1983. Zircon saturation revisited: temperature and composition effects in a variety of crustal magma types. Earth Planet. Sci. Lett. 64, 295–304.
Willner, A.P., Krohe, A., Maresch, W.V., 2000. Interrelated P-T-t-d paths in the Variscan Erzgebirge Dome (Saxony, Germany): Constraints on the rapid exhumation of high-pressure rocks from the root zone of a collisional orogen. Int. Geol. Rev. 42, 64–85.
Wolf, M., Romer, R.L., Franz, L., López-Moro, F.J., 2018. Tin in granitic melts: the role of melting temperature and protolith composition. Lithos 310–311, 20–30.
Xing, K., Shu, Q.H., Lentz, D.R., 2021. Constraints on the formation of the giant Daheishan porphyry Mo deposit (NE China) from whole-rock and accessory mineral geochemistry. J. Petrol. 62 https://doi.org/10.1093/petrology/egab018.
Xu, B., Jiang, S.Y., Wang, R., Ma, L., Zhao, K.D., Yan, X., 2015. Late Cretaceous granites from the giant Dulong Sn-polymetallic ore district in Yunnan Province, South China: Geochronology, geochemistry, mineral chemistry and Nd–Hf isotopic compositions. Lithos 218–219, 54–72.
Xu, R., Romer, R.L., Glodny, J., 2021. External fluids cause alteration and metal redistribution in the granite-hosted Tangziwa Sn-Cu deposit, Gejiu district. China. Lithos 382–383, 105937.
Yang, L., Wang, Q.F., Groves, D.I., Lu, S., Li, H.J., Wang, P., Deng, J., 2021. Multiple orogenic gold mineralization events in a collisional orogen: Insights from an extruded terrane along the southeastern margin of the Tibetan Plateau. J. Struct. Geol. 147, 104333.
Yang, Q., Xia, X.P., Zhang, W.F., Zhang, Y.Q., Xiong, B.Q., Xu, Y.G., Wang, Q., Wei, G.J., 2018. An evaluation of precision and accuracy of SIMS oxygen isotope analysis. Solid Earth Sciences 3, 81–86.
Yuan, S.D., Williams-Jones, A.E., Romer, R.L., Zhao, P.L., Mao, J.W., 2019. Protolith-related thermal controls on the decoupling of Sn and W in Sn-W metallogenic provinces: Insights from the Nanling Region, China. Econ. Geol. 114, 1005–1012.
Zhang, B.L., Lv, G.X., Su, J., Shen, S.L., Liu, R.L., Liu, J.G., Hai, L.F., Zhang, G.L., 2015. A study of the tectono-lithofacies mineralization regularities of the Gejiu tin-polymetallic orefield, Yunnan, and prospecting in its western part. Earth Sci. Front. 22, 78–87 in Chinese with English abstract.
Zhang, S.B., Zheng, Y.F., Wu, Y.B., Zhao, Z.F., Gao, S., Wu, F.Y., 2006. Zircon U-Pb age and Hf-O isotope evidence for Paleoproterozoic metamorphic event in South China. Precambr. Res. 151, 265–288.
Zhang, Y., Huang, Z.L., Luo, T.Y., Qian, Z.K., Zhang, J.W., Sun, J.B., 2013. The geochemistry and SIMS U-Pb zircon dating of the Jiasha gabbric-monzonitic intrusion in Gejiu district, Yunnan Province. Geochimica 42, 523–543 in Chinese with English abstract.
Zhang, Y., Huang, Z.L., Luo, T.Y., Qian, Z.K., 2011. LA-ICP-MS Zircon U-Pb dating and petrogenesis of Shenxianshui granite in Gejiu, Yunnan Province, China. Acta Mineralogica Sinica 31, 515–524 in Chinese with English abstract.
Zhang, Y.H., Zhou, J.X., Tian, S.C., Li, H.M., Hao, S., Jiang, Y.G., He, X.H., 2020. Genesis of the oxidized Sn ores in the Gejiu district, Yunnan Province. SW China. Ore Geology Reviews 121, 103474.
Zhao, J., Zuo, R., Chen, S., Kreuzer, O.P., 2015. Application of the tectono-geochemistry method to mineral prospectivity mapping: a case study of the Gaosong tin-polymetallic deposit, Gejiu district, SW China. Ore Geol. Rev. 71, 719–734.
Zhong, L.X., 2015. Geochemical characteristics, diagenetic ages and tectonic significances of the intermediate-felsic intrusive rocks in Qinghai Lajishan mountains. Doctoral thesis, China University of Geosciences, Beijing (in Chinese with English abstract).
Zhou, L.M., Wang, R., Hou, Z.Q., Li, C., Zhao, H., Li, X.W., Qu, W.J., 2018. Hot Paleocene-Eocene Gangdese arc: Growth of continental crust in southern Tibet. Gondwana Res. 62, 178–197.
Zi, J.W., Cawood, P.A., Fan, W.M., Wang, Y.J., Tohver, E., McCuaig, T.C., Peng, T.P., 2012. Triassic collision in the Paleo-Tethys Ocean constrained by volcanic activity in SW China. Lithos 144, 145–160.
Ziegler, P.A., Dèzes, P., 2006. Crustal evolution of western and central Europe. Geological Society, London, Memoirs 32, 43–56.